arXiv:2201.02775v3 [cs.CR] 11 Apr 2023

ADI: Adversarial Dominating Inputs in Vertical Federated Learning Systems

Qi Pang[†1], Yuanyuan Yuan[‡], Shuai Wang[‡2], Wenting Zheng[†]
[†]Carnegie Mellon University, [‡]HKUST

***Abstract*—Vertical federated learning (VFL) system has recently become prominent as a concept to process data distributed across many individual sources without the need to centralize it. Multiple participants collaboratively train models based on their local data in a privacy-aware manner. To date, VFL has become a de facto solution to securely learn a model among organizations, allowing knowledge to be shared without compromising privacy of any individuals.**

Despite the prosperous development of VFL systems, we find that certain inputs of a participant, named adversarial dominating inputs (ADIs), can dominate the joint inference towards the direction of the adversary's will and force other (victim) participants to make negligible contributions, losing rewards that are usually offered regarding the importance of their contributions in federated learning scenarios.

We conduct a systematic study on ADIs by first proving their existence in typical VFL systems. We then propose gradient-based methods to synthesize ADIs of various formats and exploit common VFL systems. We further launch greybox fuzz testing, guided by the saliency score of "victim" participants, to perturb adversary-controlled inputs and systematically explore the VFL attack surface in a privacy-preserving manner. We conduct an in-depth study on the influence of critical parameters and settings in synthesizing ADIs. Our study reveals new VFL attack opportunities, promoting the identification of unknown threats before breaches and building more secure VFL systems.

***Index Terms*—vertical federated learning, adversarial example, fuzz testing**

I. Introduction

A traditional machine learning system workflow involves a data pipeline, which uses a central server that hosts the trained model to make predictions. Thus, all data collected by local devices and sensors are sent to the central server for model training and making predictions. This data integration technique necessitates users sharing their data with a central server, which is strongly opposed due to a variety of real-world concerns, including data privacy, industrial competition, and complex administrative procedures.

To address this problem, federated learning (FL) [101] retains private data locally to train intermediate models. The parameters of these locally trained intermediate models are then aggregated into a single, consolidated, and gradually improved global model. Model aggregation uses either a trusted central coordinator or cryptographic techniques such as secure multi-party computation (MPC) [38]. Unlike centralized machine learning, FL shares parameters rather than sensitive data, hence alleviating privacy leakage. Moreover,

[1]Majority of the work is done when Qi Pang was at HKUST.
[2]Corresponding author.

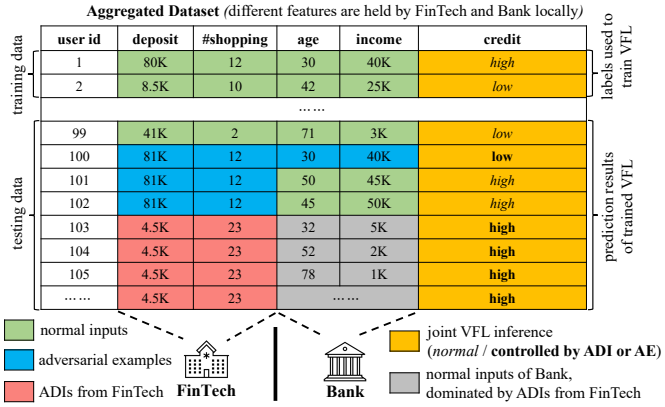


Fig. 1: ADIs from FinTech dominate the VFL predictions.

depending on how local data are distributed, FL systems can be classified into *vertical federated learning* (VFL) [46, 101] and *horizontal federated learning* (HFL) [18, 69]. In HFL, participants possess different data samples in the same feature space, e.g., Google users jointly use their own local keystroke data to train a global, remote model [45]. VFL participants are often companies/institutions owning a subset of the feature space. Fig. 1 presents a typical vertical federated logistic regression (HeteroLR) scenario [46]. In normal usage (the green data), FinTech $\mathcal{A}$ holds a a subset of the features for a group of users, whereas Bank $\mathcal{B}$ holds another subset of the features for the same users. $\mathcal{A}$ and $\mathcal{B}$ jointly predict a user's credit score (high/low) without leaking each participant's local data to the other participants.

Despite encouraging development of FL for aggregating dispersed data across participants, emerging attacks targeting this new computing paradigm have been revealed. The distribution of the training process to a set of potentially malicious clients creates backdoor attack or adversarial example (AE) opportunities on the shared model [12, 17, 85, 92, 94, 99]. While practical attacks have been proposed toward HFL [12, 17, 99], attack on VFL have not been systematically studied.

This research examines security issues of VFL in light of its growing adoption in security- and privacy-sensitive domains such as credit scoring, insurance, and loan assessment [101]. Particularly, we find that a set of unique inputs, which we call *adversarial dominating inputs* (ADIs), manipulate the joint predictions of a well-trained VFL model. When ADIs are used by a malicious participant, other benign participants' contributions to the joint prediction are nullified. Again, considering

Fig. 1, we find that by perturbing $\mathcal{A}$'s data into ADIs (red in Fig. 1), $\mathcal{A}$ controls the joint prediction to a fixed answer at their will, and diminishes the influence of $\mathcal{B}$'s data (grey in Fig. 1). As a comparison, an adversarial example (AE), marked in blue in Fig. 1, only misclassifies one input from Bank $\mathcal{B}$ when it is used by FinTech $\mathcal{A}$. When $\mathcal{B}$ uses different inputs, the joint inference returns normal. In short, AEs fail to constantly manipulate VFL inferences, and AEs do not diminish benign participants' contribution explicitly.

This research, as the first systematic study on ADIs in VFL, is motivated by findings in Fig. 1. We first formulate ADIs and prove their existence in common VFL protocols. Then, in two steps, we explore ADIs in real-world VFL systems. First, we design gradient-based approaches for ADI synthesis in a *blackbox* setting. Second, inspired by feedback-driven software fuzzing, we design a *greybox* fuzz testing framework to uncover ADIs. The proposed two-step approaches delineate attack vectors using ADIs from different perspectives and at varying costs: gradient-based methods demonstrate an end-to-end, practical exploitation using ADIs from an adversarial participant, whereas fuzzing enables in-house vulnerability assessment to comprehensively uncover ADIs in a privacy-preserving manner under all VFL participants' collaboration.

Our evaluation includes three popular VFL systems with various input formats (e.g., images, tabular data). We achieve promising success rates of gradient-based ADI synthesis and illustrate the stealth of synthesized ADIs by comparing them with normal inputs. We also find 2,320 ADIs over 92 hours of fuzzing in total, revealing large attack surfaces of popular VFL systems. We investigate how several key parameters and settings can influence ADI synthesis and uncovering. Overall, we show that the ADI issue is a crucial but often neglected impediment in adopting VFL in real-world circumstances. In sum, this study makes the following contributions:

- We identify ADIs, as a novel generalization of AEs in the context of VFL. ADIs constantly dominate the joint inference made by VFL, and extensively diminish other participants' contribution to model inference, thus hogging the rewards provided to incentivize VFL participants contributing important features.
- We prove the existence of ADIs in popular VFL systems. We propose gradient-based methods for ADI synthesis. We design a fuzzing tool to comprehensively uncover ADIs and facilitate vulnerability assessment of VFL systems. Our method is adaptable to various VFL systems and input formats.
- We achieve high success rates of generating ADIs to exploit VFL systems, indicating that ADIs are prevalent yet neglected issues. Our insights can provide users with the up-to-date understanding of VFL systems.

We publicly maintain our artifact at [4].

II. Background

VFL Overview. In VFL, each participant learns from distinct feature partitions within a same data sample. Given two participants $\mathcal{A}$ and $\mathcal{B}$, features X^i of a data sample i are partitioned into $X^i_\mathcal{A}$ and $X^i_\mathcal{B}$ ($X^i = X^i_\mathcal{A} || X^i_\mathcal{B}$; $||$ is the concatenation) and possessed separately by $\mathcal{A}$ and $\mathcal{B}$. As shown in Fig. 1, a regional FinTech and a bank located in the same region maintain records of many local residents. To predict a resident i's credit score, the FinTech and the bank can extract i's financial records and make the joint inference. Although data maintained by the FinTech and the bank have very different feature spaces, they belong to the same user i. The prediction results will be aggregated in a coordinator $\mathcal{C}$ (omitted in Fig. 1) and returned to $\mathcal{A}$ and $\mathcal{B}$.

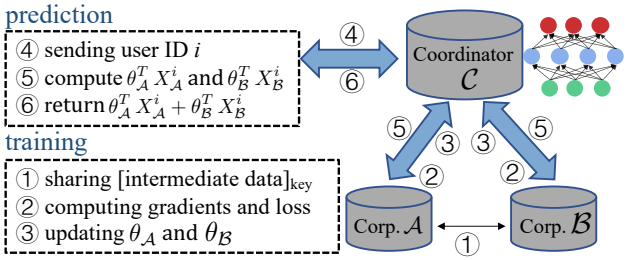


Fig. 2: Architecture of a VFL system.

During training, VFL participants exchange intermediate information and compute training losses and gradients in a privacy-aware manner, where raw data are kept locally by each participant. Fig. 2 depicts a typical VFL scenario, where $\mathcal{A}$ and $\mathcal{B}$ jointly train a model. $\mathcal{A}$ also possesses the corresponding labels. Some VFL systems also employs a coordinator $\mathcal{C}$. Holistically, model training is divided into three steps: 1) $\mathcal{A}$ and $\mathcal{B}$ encrypt and exchange the intermediate stages for gradient and loss calculations; 2) $\mathcal{A}$ and $\mathcal{B}$ compute the encrypted gradients, and $\mathcal{A}$ computes the loss and uploads the encrypted gradients and losses to $\mathcal{C}$; and 3) $\mathcal{C}$ decrypts the gradients and updates the models' parameters $\theta_\mathcal{A}$ and $\theta_\mathcal{B}$, and then sends them back to $\mathcal{A}$ and $\mathcal{B}$.

To use a trained VFL, common user IDs $i \in I$ shared by $\mathcal{A}$ and $\mathcal{B}$ must be first confirmed [80]. The corresponding records will be extracted (④ in Fig. 2), and each participant will compute the local intermediate results which will be aggregated in $\mathcal{C}$ (⑤ in Fig. 2). $\mathcal{C}$ will compute the joint prediction result and return it to $\mathcal{A}$ and $\mathcal{B}$ (⑥ in Fig. 2).

VFL vs. HFL. As noted in Sec. I, HFL generally refers to the FL setting where participants hold different samples of the same features, and they jointly train a central model. In contrast, VFL is originated from the practical needs that companies and institutions owning fragmented data belonging to the same group of users, and they compensate each other and maximize data utilization through collaborative model training and predictions. That is, training/test data in VFL participants are from distinct feature spaces of the same users, and each VFL participant has its own unique local model. To date, most real-world VFL designs have 2 (maximum 4) participants [27, 64, 98, 101]. We clarify that ADIs, as introduced in Sec. III, particularly exist in VFL. Since each HFL participant receives the full model from the central server, a participant does not rely on other participants to make predictions at the

inference stage. Thus, in HFL, predictions on a participant cannot be influenced and dominated by malicious participants at the inference stage. Sec. III-A presents further comparison between ADIs and adversarial examples in HFL.

Learning Protocols. We introduce two popular VFL systems: vertical federated logistic regression (HeteroLR) [46] and vertical federated neural network (SplitNN) [44]. They are widely used in real-world VFL scenarios and show comparable performance with their centralized versions. More importantly, most parameter-based learning methods in VFL can be extended from these two core protocols. For instance, the vertical federated visual question answering (VFVQA), a popular paradigm facilitating answering questions about images [58], is extended from SplitNN. Hence, our proof on ADI existence (Sec. III-C) and evaluation (Sec. VII) consider SplitNN and HeteroLR. We also implement and evaluate VFVQA by extending SplitNN. In short, our study subsumes regression, classification, and VQA tasks offered by VFL systems. We present the training and implementation details of all three protocols in Appx. I and discuss tree-based VFL systems in Appx. C.

To help readers better understand VFL systems, we present Fig. 3, which depicts the architecture of heterogeneous neural network (also known as a special case of SplitNN). SplitNN facilitates multiple participants holding data with different feature spaces to train a distributed model without sharing raw data. In the forward propagation phase, $\mathcal{A}$ and $\mathcal{B}$ compute the outputs of their local models ($w_{\mathcal{A}}$ and $w_{\mathcal{B}}$) and forward them to the coordinator $\mathcal{C}$:

$$L_{\mathcal{A}} = f_{\mathcal{A}}(X_{\mathcal{A}}, w_{\mathcal{A}}),\ L_{\mathcal{B}} = f_{\mathcal{B}}(X_{\mathcal{B}}, w_{\mathcal{B}}) \tag{1}$$

The forwarded local outputs, $L_{\mathcal{A}}$ and $L_{\mathcal{B}}$, will be concatenated on the coordinator side and fed to the coordinator model ($w_{\mathcal{C}}$) for a joint inference whose result is $L_{\mathcal{C}}$.

$$L_{\mathcal{C}} = f_{\mathcal{C}}([L_{\mathcal{A}} \,||\, L_{\mathcal{B}}], w_{\mathcal{C}}) \tag{2}$$

In the backward propagation phase, the coordinator $\mathcal{C}$ computes the gradients $f'_{\mathcal{C}}(L_{\mathcal{C}})$, performs gradient descent on its model, and obtains the gradients of local outputs submitted by the participants as follows:

$$[\nabla l(L_{\mathcal{A}}; w_{\mathcal{C}}) \,||\, \nabla l(L_{\mathcal{B}}; w_{\mathcal{C}})] = f'_{\mathcal{C}}(L_{\mathcal{C}}) \tag{3}$$

Back to the participant side, once receiving the gradients, the participants further compute the local gradients $f'_{\mathcal{A}}(\nabla l(L_{\mathcal{A}}; w_{\mathcal{C}}; X_{\mathcal{A}}))$ and $f'_{\mathcal{B}}(\nabla l(L_{\mathcal{B}}; w_{\mathcal{C}}; X_{\mathcal{B}}))$, and then update local models. f represents the neural network and f' represents its derivative. In the forward and backward propagations, no raw data is directly sent to the coordinator or exchanged among participants, and all intermediate data is encrypted. Furthermore, by extending the SplitNN protocol, we can construct more complex models like CNN and LSTM following the VFL paradigm.

VFL Reward. VFL enables an individual participant (e.g., a bank) to enrich its data and maximize data utilization by incorporating data from other participants. Participants will be rewarded for their contributions to the joint inference as is standard in collaborative learning and federated learning. Participants are often rewarded following a "pay-per-use" model [67, 82, 89, 103], where participants are compensated according to the *importance* of their contributed data in each joint prediction [63, 96].

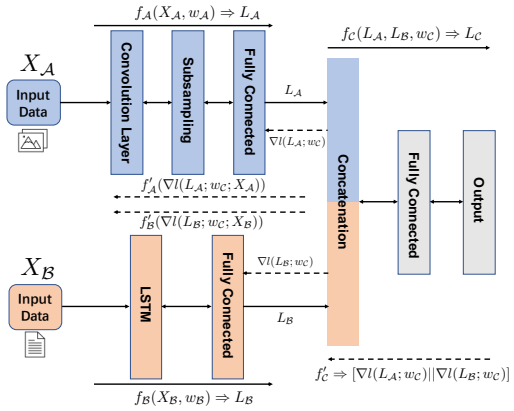


Fig. 3: Architecture of SplitNN.

III. Related Work and Problem Statement

A. FL Security and ADI Positioning

Distributed Machine Learning. Advances in distributed machine learning systems have enabled large-scale machine learning algorithms to be run in a distributed manner [20, 26, 54, 76, 78, 93]. Horizontal federated learning was developed to provide an efficient and privacy-aware approach for distributed machine learning [69], in which clients only share model updates rather than training data. The concept of federated learning is expanded further into a vertical paradigm, namely VFL [46, 73, 101], in which clients hold separate features that belong to the same users.

Attacks on FL. Existing work has shown that representative deep learning attacks, such as backdoor and training data reconstruction attacks, can be launched in collaborative learning settings. Nevertheless, most existing works attack HFL [12, 17, 21, 32, 37, 72, 85, 88, 92, 94, 99]. Recent works [63, 95] conduct private training data leakage attacks via deliberately-modified gradients during VFL training. [35] launches attacks to infer labels of private training data, and [59] inserts backdoor samples. All these recent VFL attacks are launched during the VFL training phase. In contrast, this work targets the joint inference phase of well-trained VFL models. ADIs enables an adversary to control VFL joint prediction towards their will, reduce others' contribution, and hog rewards used to incentivize participants.

Hardening Federated Learning. Bonawitz et al. [19] introduce secure aggregation to defeat a semi-honest server and the dropout of arbitrary users. Pillutla et al. [77] propose a robust aggregation scheme toward corrupted client updates. FoolsGold mitigates sybil-based poisoning attacks based on the diversity of client updates [36]. Li et al. [55] enhance the fairness of resource allocation in HFL. Holistically, our present study assesses the unfair contribution of VFL participants at the inference stage and the security implications.

Connection Between ADIs and AEs. Methods generating standard AEs in centralized learning or HFL [11, 40] can also be extended to exploit VFL. And as illustrated in Fig. 1, AEs can also manipulate specific VFL predictions to the target labels. Holistically, we deem ADIs and AEs are related, in the sense that ADIs deem a novel extension of AEs in the context of VFL.

Differences Between ADIs and AEs. In the VFL scenarios, AEs and ADIs differ in the following aspects. First, ADIs aim to dominate practically all inputs from victim participants, while AEs usually misclassify a specific input to a targeted label. As shown in Fig. 1, when the victim participant takes another input, the same AE is unlikely to manipulate the prediction again. Also, in formulating the adversary's objective, AEs do not consider victim participants' contribution. In contrast, ADIs explicitly minimize the victim participants' contribution, thus hogging rewards used to incentivize collaborative learning participants contributing important features [29, 74, 84, 106, 107]. Moreover, in the context of VFL, ADIs only need to manipulate a subset of features (e.g., in Fig. 1, only FinTech's features are controlled), whereas AEs control and manipulate the full feature space. In Sec. VII-C, we empirically assess AEs in attacking VFL, and show that standard AEs are not effective in dominating VFL outputs.

ADIs vs. Other Perturbed Inputs. Existing research has proposed methods in synthesizing universal adversarial perturbation (UAP) [70]. UAP launches a synthesis procedure that causes misclassification of many images using one unified perturbation. ADIs also result in a universal misclassification. However, we clarify that "universal" in UAP and ADIs have different meanings. UAP finds a universal perturbation to misclassify many images, whereas we find ADIs from a subspace of the entire feature space to *dominate all other subspaces possessed by victim participants*. To compare with UAP, ADIs explicitly model and minimize victim participants' contributions. Also, while most UAP techniques misclassify images into arbitrary labels [22, 70], we target a specified label l_{target} (see Fig. 4), and only allow perturbing adversary-controlled feature partition $X^i_{\mathcal{A}}$ instead of the entire feature space $X^i = X^i_{\mathcal{A}}||X^i_{\mathcal{B}_1}||\cdots||X^i_{\mathcal{B}_{m-1}}$.

To empirically assess the comparison, we first generate UAPs on VFL models trained on MNIST [52], and then evaluate the dominating rates of inputs from $\mathcal{A}$ when using UAPs. The UAPs achieve a fooling rate [70] of around 90%, which is considered as effective according to [70]. However, when $\mathcal{A}$ applies UAPs on its inputs, none of the inputs can achieve a dominating threshold higher than 95% (this threshold is defined in Sec. III-D), and only 0.21% of the inputs achieve a dominating threshold higher than 90%. In contrast, when $\mathcal{A}$ uses ADIs, over 33.9% inputs can achieve a dominating threshold higher than 95% (see details in Sec. VII). More importantly, the generation of UAPs needs to iterate over the whole training dataset, which is not practical in the setting of VFL systems, where the malicious participant hardly has access to the whole training dataset.

One may wonder if adversarial participant $\mathcal{A}$ can simply use random inputs to attack. Although random inputs can affect the joint inference in an undesirable manner (and presumably reduce the VFL model accuracy), we argue that random inputs are less profitable than ADIs for two reasons. First, ADIs allow to specify an adversary-targeted label l_{target} (see Sec. IV), whereas random inputs simply "muddle" the joint prediction. More importantly, random inputs can hardly nullify benign participants' contributions, while ADIs mostly negate features contributed by benign participants, thus hogging the rewards provided to incentivize participants. We empirically compare ADI with random inputs in Sec. VII-C, whose findings are aligned with our analysis here.

B. Threat Model

Attack Scenario. This research considers m participants in a VFL system f. Our attack targets the inference phase of well-trained VFL models, *not* the training phase. We assume that in the joint inference phase, the inputs of one participant are controlled by the adversary. We refer to this adversary as $\mathcal{A}$, and the rest $m-1$ benign participants as $\mathcal{B}_j$, where $j \in \{1, \cdots, m-1\}$. We also refer to the central coordinator used by VFL as $\mathcal{C}$. The feature space X^i of a data sample i is thus partitioned into $X^i = X^i_{\mathcal{A}}||X^i_{\mathcal{B}_1}||\cdots||X^i_{\mathcal{B}_{m-1}}$ and held by different participants. To clarify, f yields the score for the target label in classification tasks, while it yeilds the regression results in regression tasks.

Adversary's Objectives. $\mathcal{A}$ aims to dominate the joint inference using ADIs and extensively diminish the contribution of other participants. This way, $\mathcal{A}$ can control the result towards the direction of their will and hog the vast majority of rewards, given that only $\mathcal{A}$ contributes non-trivial features to the joint prediction. We formally define ADIs as following:

Definition 1 (ADIs)**.** *Consider VFL system f with m participants: $f(X_{\mathcal{A}}, X_{\mathcal{B}_1}, \cdots, X_{\mathcal{B}_{m-1}})$, an input $X^*_{\mathcal{A}}$ is regarded as an ADI when the output of the VFL system is not influenced by changing the inputs from participants $\mathcal{B}_j$, where $j \in \{1, \cdots, m-1\}$. Formally, we regard $X^*_{\mathcal{A}}$ as an ADI when the following holds:*

$$\mathbb{V}_{X_{\mathcal{B}} \in D_{\mathcal{B}}}(f(X^*_{\mathcal{A}}, X_{\mathcal{B}_1}, \cdots, X_{\mathcal{B}_{m-1}})) \leq \epsilon\,, \tag{4}$$

where ϵ is a small value, $\mathbb{V}$ represents the variance, and $X_{\mathcal{B}} \in D_{\mathcal{B}}$ is short for $X_{\mathcal{B}_1} \in D_{\mathcal{B}_1}, \cdots, X_{\mathcal{B}_{m-1}} \in D_{\mathcal{B}_{m-1}}$.

Eq. 4 illustrates that $X^*_{\mathcal{A}}$ becomes an ADI when the output variance is bounded by ϵ w.r.t. the change of inputs from $\mathcal{B}_1, \cdots, \mathcal{B}_{m-1}$. This way, $\mathcal{A}$ *dominates* the joint prediction, no matter what inputs are used by other participants.

Adversary's Capability & Assumptions. We assume that adversary $\mathcal{A}$ can arbitrarily perturb its inputs to generate ADIs. And in the VFL joint inference stage, all inputs of $\mathcal{B}$ follow the distribution of their training dataset. To generate ADIs, we assume that in the *joint inference phase*, $\mathcal{A}$ provides a *tiny* collection of data samples to $\mathcal{B}$, which are used as $\mathcal{B}$'s test inputs. We refer to this *tiny* data sample collection as $\mathcal{S}$. $\mathcal{S}$ does not deviate from the distribution of $\mathcal{B}$'s standard inputs.

We find that to generate ADIs that dominate at least 95% of inputs in $\mathcal{B}$ (threshold "95%" is clarified in Sec. III-D), we only need a tiny $\mathcal{S}$ whose elements are randomly selected from the test dataset of $\mathcal{B}$. $\mathcal{S}$ is never revealed to $\mathcal{B}$ during training. Sec. VII reports that we require only 20 MNIST images (i.e., 0.03% of MNIST) to dominate 95% of its standard test inputs. We study how $|\mathcal{S}|$ influences ADI synthesis in Appx. D and discuss the selection of $\mathcal{S}$ in Appx. C.

Additionally, we show that $\mathcal{A}$ can successfully generate ADIs even without accessing the inputs of $\mathcal{B}$. Instead, $\mathcal{A}$ only knows the *input range* of $\mathcal{B}$'s inputs. This observation makes the ADI generation algorithm more practical and further enhances the technical feasibility and stealthiness in real-world attacks. See evaluations in Sec. VII-E.

Sec. III-C proves the existence of ADIs in VFL. We assume that the probability density function of the benign participants' data can be approximated by Gaussian Mixture Models (GMMs) [68], which is aligned with the conventions [15, 33, 49, 53, 66, 108] in machine learning. This assumption is reasonable as GMMs have the power to approximate any smooth distributions [39]. We also prove for the non-smooth distribution scenario in Appx. A.

Examples and Feasibility Clarification. Consider the VFL example in Fig. 1, where a bank and a FinTech jointly predict a user's credit score. An adversarial FinTech can use ADIs to control the joint inference; for instance, the joint inference can be forced to always yield high credit scores, despite poor financial records ("income" in Fig. 1) the users may have in the bank. Given a well-trained VFL model, we assume that it is feasible for $\mathcal{A}$ to provide the tiny collection of data samples $\mathcal{S}$ in the following way: $\mathcal{A}$ can conspire with a *small* group of users who behave normally when generating the data to form $\mathcal{S}$. These users submit $\mathcal{S}$ to $\mathcal{B}$ and also disclose $\mathcal{S}$ to $\mathcal{A}$ (see Appx. J for an end-to-end diagram of this strategy). We envision that regular VFL participants (e.g., banks) would not refuse to take S as *test* inputs, especially considering its tiny size.

ADI Synthesis and Discovery. We first propose an ADI synthesis attack in the blackbox setting, which is launched during the inference phase of well-trained VFL models. The ADI synthesis is based on gradients, which are estimated with finite difference method (FDM) [42] in the blackbox setting. The adversarial participant $\mathcal{A}$ only needs to know the current input index (i.e., user ID) and observes the VFL inference results, which is a common setting in VFL. $\mathcal{A}$ has no access to model $M_{\mathcal{B}}$ or $\mathcal{B}$'s private training data.

We also propose a fuzz testing framework to discover ADIs (Sec. V). Fuzzing helps VFL developers comprehensively discover ADIs and perform quantitative security assessment (which is hardly feasible for our blackbox approach given the privacy consideration; see Table I). For fuzzing, $\mathcal{A}$ does not need to access $\mathcal{S}$. Instead, participants share a saliency score to guide fuzzing (comparable to how code coverage guides software fuzzing [105]). This saliency score is a number derived from the saliency map's l_1 norm. That is, to protect participants' data privacy, information of *low sensitivity* is shared instead of the entire saliency maps.

TABLE I: $\mathcal{A}$'s accessibility under different schemes.

	Blackbox ADI Synthesis	Greybox Fuzz Synthesis
$\mathcal{B}$**'s model**	×	×
$\mathcal{B}$**'s traing dataset**	×	×
***tiny* test dataset** $\mathcal{S}$[1]	✓	×
low-sensitivity saliency score of $\mathcal{B}$	NA	✓
Collaboration of all participants	×	✓

[1] $\mathcal{A}$ feeds $\mathcal{S}$ to $\mathcal{B}$ by conspiring with a few users, as clarified in threat model. In our implementation, $\mathcal{S}$ comprises a few random samples from $\mathcal{B}$'s test dataset.

We summarize assumptions in Table I, where ✓ means that $\mathcal{A}$ requires the corresponding accessibility. Greybox fuzzing is guided by saliency scores, whereas blackbox ADI synthesis denotes a lightweight generation process under objectives. We clarify details of two approaches in Sec. IV and Sec. V, respectively. Readers may also refer to Appx. J for an end-to-end illustration of blackbox ADI synthesis procedures. And we also evaluate the scenario where $\mathcal{A}$ cannot access $\mathcal{S}$ in Sec. VII-E.

C. Proof on the Existence of ADIs in VFL

Below, we prove that ADIs exist in two VFL systems: HeteroLR and SplitNN. As noted in Sec. II, most parameterized VFL systems (e.g., VFVQA) can be extended from them. Sec. III-D discusses the generalization. Below, we consider two participants and discuss extension to more participants in Sec. III-D.

Variance Bound for VFL Systems. Participant $\mathcal{A}$ holds the data $X_{\mathcal{A}} \in D_{\mathcal{A}}$, whereas participant $\mathcal{B}$ holds the data $X_{\mathcal{B}} \in D_{\mathcal{B}}$ following any distribution whose density function is $p(X_{\mathcal{B}})$. As noted in our threat model, we make an reasonable assumption that this density function can be approximated by GMMs. $\mathcal{A}$ is controlled by an adversary, whereas $\mathcal{B}$ behaves normally. The VFL system f takes $X_{\mathcal{A}}$ and $X_{\mathcal{B}}$ as inputs, and its output can be expressed as $f(X_{\mathcal{A}}, X_{\mathcal{B}})$, where $X_{\mathcal{A}} \in \mathbb{R}^{d_1}$, $X_{\mathcal{B}} \in \mathbb{R}^{d_2}$, and d_1, d_2 denote dimensions of the features in $\mathcal{A}$ and $\mathcal{B}$. Same as Def. 1, f yields the score for the target label in classification tasks, and the regression results in regression tasks. We present the output variance bound of the VFL system:

Corollary 1 (Variance Bound of VFL systems)**.** *With fixed input $X^*_{\mathcal{A}}$ and varying input $X_{\mathcal{B}}$ following any distribution $D_{\mathcal{B}}$ whose density function is $p(X_{\mathcal{B}})$. For any ϵ, there exists $X^*_{\mathcal{A}}$ that the output variance of the VFL system (SplitNN, HeteroLR, and their extensions) with respect to $X_{\mathcal{B}} \in D_{\mathcal{B}}$ is bounded by ϵ:*

$$\mathbb{V}_{X_{\mathcal{B}} \in D_{\mathcal{B}}}(f(X^*_{\mathcal{A}}, X_{\mathcal{B}})) \leq \epsilon$$

According to Cor. 1 and Def. 1, the ADI $X^*_{\mathcal{A}}$ exists for VFL systems. We present detailed proof of Cor. 1 for the widely used VFL systems of HeteroLR and SplitNN in Appx. A.

D. Extension & Practical Consideration

Generalization. Sec. II has clarified that most parameter-based VFL systems are extensions of HeteroLR and SplitNN. These models all concatenate features from the same data

sample to form a joint inference. Thus, we assume that Cor. 1 and our proof in Appx. A subsumes most real-world cases because most parameter-based VFL systems are extensions of HeteroLR and SplitNN. Our evaluation (Sec. VII) also attacks VFVQA, an extension of SplitNN. We also discuss attack tree-based VFL in Appx. C.

Bounded Mutation. We have proved the existence of ADIs when arbitrarily mutating $X^*_{\mathcal{A}}$. Nevertheless, arbitrary mutation can generate unrealistic ADIs, which may not be desirable in real-world exploitations. We design a bounded mutation scheme to generate more realistic inputs. Bounded mutation perturbs $X^*_{\mathcal{A}}$ within a predefined range. In this paper, we perturb $X^*_{\mathcal{A}}$ within its variance in the standard input dataset on $\mathcal{A}$. Note that "variance" in bounded mutation is obtained from the standard inputs on $\mathcal{A}$. Variance of standard inputs on $\mathcal{B}$ is *not* needed. We also prove the existence of ADIs under bounded mutation in Appx. B. The generated ADIs are seen as indistinguishable from normal inputs, indicating a severe, practical, yet overlooked issue to VFL. We empirically evaluate the stealth of ADIs generated by bounded mutation in Sec. VII-A and Sec. VII-B.

More Participants. As introduced in threat model (Sec. III-B), we use ADIs to attack a VFL system of m participants, where m can be greater than two. While Cor. 1 is based on two participants $\mathcal{A}$ and $\mathcal{B}$, our proofs can be easily extended to multi-participant VFL systems. To do so, features on $m-1$ benign participants $\mathcal{B}$ can be first aggregated into $X_{\mathcal{B}}$ to bridge with Cor. 1. We also empirically assess the presence of ADIs with various numbers of malicious and benign participants in Appx. G and Appx. H.

Practical Assessment of ADIs. Despite the inherent existence of ADIs in VFL, it is difficult to obtain a complete view of $\mathcal{B}$'s inputs. Hence, we use the following practical assessment to decide if $X^*_{\mathcal{A}}$ denotes an ADI:

Definition 2 (Practical Assessment of ADIs)**.** *Consider VFL with m participants, $F(X_{\mathcal{A}}, X_{\mathcal{B}_1}, \cdots, X_{\mathcal{B}_{m-1}})$. F outputs prediction label with the largest score. An input $X^*_{\mathcal{A}}$ is an ADI when the VFL joint prediction is not influenced by changing the inputs from participants $\mathcal{B}$. Formally:*

$$r(X^*_{\mathcal{A}}) = \frac{\sum_{i=1}^{n} \mathbb{I}(F(X^*_{\mathcal{A}}, X^i_{\mathcal{B}_1}, \cdots, X^i_{\mathcal{B}_{m-1}}) = l_{target})}{n} \geq x\% \ ,$$

where r computes the dominated proportion of $\mathcal{B}$'s inputs for $X^*_{\mathcal{A}}$, $x\%$ is the dominating threshold, n is the samples' number in test dataset, and $\mathbb{I}(msg) = 1$, if msg is true, otherwise, $\mathbb{I}(msg) = 0$.

Our study adopts this practical assessment, where an input of $\mathcal{A}$ deems an ADI if the joint inference is confined as an attacker-specified label l_{target} for $x\%$ of the data samples in the standard input dataset of $\mathcal{B}$. x is empirically decided as 95 and 99, indicating that an ADI can extensively dominate 95% and 99% of the inputs from $\mathcal{B}$, respectively.

This section has formulated the research problem and presented discussions from various aspects. Sec. IV describes gradient-based algorithms to synthesize ADIs. Sec. V proposes a fuzz testing-based approach to uncovering ADIs.

Algorithm 1 Gradient-Based ADI Synthesis.

1: **function** ***Saliency_est***$(X^*_{\mathcal{A}}, X^i_{\mathcal{B}}, M)$
2: $output \leftarrow M(X^*_{\mathcal{A}}, X^i_{\mathcal{B}})$
3: $saliency \leftarrow ||\frac{\partial Var(output)}{\partial X^i_{\mathcal{B}}}||_1$
4: **return** $saliency$
5: **function** ***ADI_generation***$(X^*_{\mathcal{A}}, M, l_{target}, Strategy, \mathcal{S})$
▷ r: computes dominated proportion of $\mathcal{B}$'s inputs as defined in Def. 2
▷ $x\%$, T: desired dominating threshold and maximum round
▷ $\alpha, \beta, \gamma, \sigma$: weight parameters
▷ $\mathbf{\Lambda}$, V, δ_t: mutation constrain, total mutation, mutation in round t
▷ $loss(X^i_{\mathcal{A}}, X^i_{\mathcal{B}}, M, l)$: loss between $M(X^i_{\mathcal{A}}, X^i_{\mathcal{B}})$ and label l
6: $V \leftarrow 0$, $\delta_1 \leftarrow 0$, $t \leftarrow 1$
7: **while** $r(X^*_{\mathcal{A}}) \leq x\%$ and $t \leq T$ **do**
8: **for** each $X^t_{\mathcal{B}} \in \mathcal{S}$ **do**
9: **if** $Strategy$ is RANDOM **then**
10: $\delta_t \leftarrow \arg\min_{\delta_t} \alpha$ ***Saliency_est***$(X^*_{\mathcal{A}} + V + \delta_t, X^t_{\mathcal{B}}, M)$ $+ \beta\, loss(X^*_{\mathcal{A}} + V + \delta_t, X^t_{\mathcal{B}}, M, l_{target})$
11: **else**
12: $\delta_t \leftarrow \arg\min_{\delta_t} \alpha$ ***Saliency_est***$(X^*_{\mathcal{A}} + V + \delta_t, X^t_{\mathcal{B}}, M)$ $+ \beta\, loss(X^*_{\mathcal{A}} + V + \delta_t, X^t_{\mathcal{B}}, M, l_{target})$ $+ \gamma\, ||\delta_t||_2 \quad$ s.t. $|V + \delta_t| \leq \mathbf{\Lambda}$
13: $\delta_t \leftarrow \sigma\, \delta_{t-1} + \delta_t$, $V \leftarrow V + \delta_t$, $t \leftarrow t + 1$
14: **return** $X^*_{\mathcal{A}} + V$

IV. Blackbox ADI Synthesis

This section proposes a blackbox, gradient-based ADI synthesis algorithm in line with our threat model in Sec. III-B. Inputs of $\mathcal{A}$ are mutated by the adversary, who aims to dominate the joint inference and minimize $\mathcal{B}$'s contribution. To assist ADI synthesis, $\mathcal{A}$ can use a tiny collection of data samples $\mathcal{S}$ aligned with the distribution of $\mathcal{B}$'s normal inputs.

Clarification. To *ease understanding*, we start by presenting a whitebox ADI synthesis algorithm, where $\mathcal{A}$ is assumed to access the gradients of the trained models in $\mathcal{B}$. Then, aligned with our threat model, we discuss turning the whitebox setting into a blackbox attack by estimating gradients.

Alg. 1 formulates ADI generation as an optimization problem. **ADI_GENERATION** is the main entry point of our algorithm, which takes the adversary-controlled input $X^*_{\mathcal{A}}$, jointly trained model M, adversary-targeted label l_{target}, the tiny collection of data samples $\mathcal{S}$, and a mutation strategy $Strategy$ as the inputs. It returns the synthesized ADI $X^*_{\mathcal{A}}+V$, where V is the mutation vector over $X^*_{\mathcal{A}}$.

Mutation Methods. **ADI_GENERATION** requires to specify mutation strategies (i.e., random vs. bounded mutation) and proceed accordingly (lines 9–12 in Alg. 1). Given an input $X^*_{\mathcal{A}}$, random mutation perturbs it in all directions, whereas bounded mutation perturbs it in a predefined range. Bounded mutation is more conservative, such that the value of mutated $X^*_{\mathcal{A}}$ is confined in a reasonable range. Although defining a "reasonable" range for arbitrary $X^*_{\mathcal{A}}$ is challenging, we specify that mutations must be bounded by the variance of this feature in the training dataset. We solve the optimization problem using projected gradient descent [9].

Random mutation aims to minimize the output loss on a target label and the contribution of inputs in $\mathcal{S}$ (line 10 in

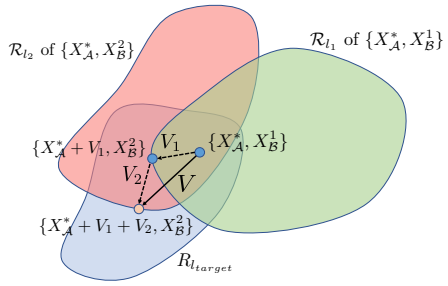


Fig. 4: A schematic view of ADI generation.

Alg. 1; see below for the description of SALIENCY_EST). In contrast, bounded mutation adds a penalty on the mutation to the objective (line 12 in Alg. 1). To facilitate a faster convergence, we use momentum (lines 13 in Alg. 1) to help accelerate updates in the right directions. Our evaluation, as will be reported in Table IV, empirically compares these two mutation strategies. As expected, random mutation manifests a higher chance of generating ADIs, whereas bounded mutations induce more stealthy ADIs (see the case studies in Sec. VII). ADI_GENERATION supports both mutation schemes and the users can select the one that best suits their needs.

Estimating Contributions of $\mathcal{B}$. SALIENCY_EST computes the saliency score, denoting the contribution of $X^i_{\mathcal{B}}$ in a joint inference. We first calculate the derivative of the output's variance for $X^i_{\mathcal{B}}$, whose l_1 norm is derived to estimate its saliency (line 3 in Alg. 1). Note that in binary classification, the output vector contains the prediction score for only one category, then we compute the derivative of the output for $X^i_{\mathcal{B}}$ directly. A lower saliency score means that a modest change in $X^i_{\mathcal{B}}$ has minimal effect on the output, implying a negligible contribution of $\mathcal{B}$ to the inference. This procedure aligns with the adversary's objectives in Sec. III.

A. A Schematic View of ADI Generation

Fig. 4 presents a schematic view to synthesize ADIs, where we proceed iteratively over a subset of $\mathcal{B}$'s inputs and gradually generate ADIs as the input of $\mathcal{A}$. For a normal joint inference, both $\mathcal{A}$'s and $\mathcal{B}$'s inputs make non-trivial effects: when fixing $\mathcal{B}$'s input as $X^1_{\mathcal{B}}$, perturbing $X^*_{\mathcal{A}}$ toward an ADI can form a high-dimensional classification region R_{l_1}, where the joint inference over $\{X^*_{\mathcal{A}}, X^1_{\mathcal{B}}\}$ constantly yields l_1. Similarly, input $X^2_{\mathcal{B}}$ and $X^*_{\mathcal{A}}$ can form another region R_{l_2}, whose induced inference is constantly l_2.

Let $\mathcal{S}$ be a dataset containing a non-trivial amount of $\mathcal{B}$'s input samples, we assume the presumed existence of a special classification region $\mathcal{R}_{l_{target}}$. When $\{X^*_{\mathcal{A}}, X^i_{\mathcal{B}}\}$ where $X^i_{\mathcal{B}} \in \mathcal{S}$ is inside its corresponding boundary $\mathcal{R}_{l_i}$ and meanwhile inside $\mathcal{R}_{l_{target}}$, the joint inference yields label l_i. Nevertheless, when $\{X^*_{\mathcal{A}}, X^i_{\mathcal{B}}\}$ locates within $\mathcal{R}_{l_{target}}$ while outside any other regions $\mathcal{R}_{l_{other}}$, where $l_{other} \neq l_{target}$, the joint inference yields l_{target}. Thus, given $\{X^*_{\mathcal{A}}, X^1_{\mathcal{B}}\}$ locates inside $\mathcal{R}_{l_1}$ in Fig. 4, perturbation V_1 sends the currently perturbed point, $\{X^*_{\mathcal{A}} + V_1, X^1_{\mathcal{B}}\}$, outside region $\mathcal{R}_{l_1}$ and gets inside the region $\mathcal{R}_{l_{target}}$. When further dealing with $X^2_{\mathcal{B}}$ paired with $X^*_{\mathcal{A}} + V_1$, mutation V_2 sends the perturbed point, $\{X^*_{\mathcal{A}} + V_1 + V_2, X^2_{\mathcal{B}}\}$, outside region $\mathcal{R}_{l_2}$ and gets inside the region $\mathcal{R}_{l_{target}}$. By iterating $\mathcal{S}$ and aggregating perturbation V_i into V, pairing $X^*_{\mathcal{A}} + V$ with inputs in $\mathcal{S}$ will be sent inside the region $\mathcal{R}_{l_{target}}$ but presumably outside of any other regions. We thus control the joint prediction when pairing $X^*_{\mathcal{A}} + V$ with $X^i_{\mathcal{B}} \in \mathcal{S}$. Moreover, Appx. D empirically shows that $X^*_{\mathcal{A}} + V$ generated over $\mathcal{S}$ achieves a high success rate of dominating at least 95% of $\mathcal{B}$'s inputs. We deem $X^*_{\mathcal{A}} + V$ as an ADI.

B. Gradient Estimation in the Blackbox Setting

The machine learning community has proposed blackbox gradient estimation approaches. Such methods are used in generating adversary examples [23, 50, 71, 90]. We use a gradient estimation-based approach to synthesizing ADIs, so $\mathcal{A}$ does not need to access $\mathcal{B}$'s trained models. We use the finite difference method (FDM) [42] to estimate gradient:

$$grad_{\mathcal{B}} = \frac{Var(M(X^*_{\mathcal{A}}, X^i_{\mathcal{B}} + \delta)) - Var(M(X^*_{\mathcal{A}}, X^i_{\mathcal{B}}))}{\delta},$$

where M is the joint model, $X^*_{\mathcal{A}}$ and $X^i_{\mathcal{B}}$ are the inputs fed to $\mathcal{A}$ and $\mathcal{B}$. δ denotes a small perturbation with the same dimension as $X^i_{\mathcal{B}}$. Thus, the saliency gradient in Alg. 1 (line 3) can be approximated. With other parts remaining the same in Alg. 1, we can synthesize ADIs in the blackbox setting. As mentioned in Sec. III-B, $\mathcal{A}$ only needs to provide the tiny data collection S to $\mathcal{B}$, and S is formed by $X^i_{\mathcal{B}}$ and $X^i_{\mathcal{B}} + \delta$.

Clarification. Conventional blackbox AE attacks denote an online setting [43, 50, 86], where they require attackers to iteratively query a remote model (e.g., a cloud service) with recently mutated inputs and decide further mutations with estimated gradiants. In contrast, for blackbox ADI synthesis, $\mathcal{A}$ needs to acquire the joint inference results only over $X^i_{\mathcal{B}} \in \mathcal{S}$ and $X^i_{\mathcal{B}} + \delta \in \mathcal{S}$. $\mathcal{A}$ pre-computes $\mathcal{S}$ *offline*, and as clarified in Sec. III-B, $\mathcal{A}$ then conspires with a small group of users, who submit $\mathcal{S}$ to $\mathcal{B}$ as a collection of test inputs. Therefore, we do not require the VFL to serve as a "cloud service" that actively processes unseen data (which is impractical in VFL scenarios). All data samples in $\mathcal{S}$ are computed *offline* and submitted to $\mathcal{B}$, before synthesizing ADIs. **In sum, our blackbox attack is faithfully aligned with how VFL is used in real-life scenarios**; see Appx. J for an end-to-end illustration of blackbox attack with diagrams.

V. UNCOVER ADIS WITH GREYBOX FUZZING

Motivation. We clarify that excellent research has been done on testing distributed systems [14, 62, 104]; these works primarily focus on concurrency bugs. Contrarily, we launch privacy-preserving testing in the context of federated learning to uncover ADIs. The gradient-based ADI synthesis algorithm described in Sec. IV can also be used to uncover ADIs. However, in-house quality assurance and vulnerability assessment are difficult, whose main reasons are twofold.

First, while malicious participant $\mathcal{A}$ can synthesize ADIs without accessing the model of $\mathcal{B}$ in blackbox ADI synthesis (see Sec. IV-B), the malicious participant needs to prepare a tiny dataset $\mathcal{S}$. As clarified in Sec. III-B and Sec. IV-B, $\mathcal{S}$ can be prepared by conspiring with a few users to submit $\mathcal{S}$

Algorithm 2 Saliency-Guided Greybox Fuzz Testing.

1: **function** ***IsADI***$(X^*_{\mathcal{A}}, \mathcal{S}, l_{target}, M)$
2: $\quad\mathcal{T} \leftarrow \varnothing$
3: $\quad$**for** each $X^i_{\mathcal{B}}$ in $\mathcal{S}$ **do**
4: $\quad\quad o \leftarrow M(X^*_{\mathcal{A}}, X^i_{\mathcal{B}})$
5: $\quad\quad$add o in $\mathcal{T}$
6: $\quad$**return** STABLE$(\mathcal{T}, l_{target})$
7: **function** ***Fuzzing***(Corpus of Seed Inputs $\mathcal{C}$, $M, \mathcal{S}$)
8: $\quad\mathcal{Q} \leftarrow \mathcal{C}$, $\mathcal{O} \leftarrow \varnothing$
9: $\quad$**for** 1 ... *MAX_ITER* **do**
10: $\quad\quad(X^*_{\mathcal{A}}, l_{target}) \leftarrow$ CHOOSENEXT$(\mathcal{Q})$
11: $\quad\quad p \leftarrow$ ASSIGNENERGY$(X^*_{\mathcal{A}})$
12: $\quad\quad$**for** 1 ... p **do**
13: $\quad\quad\quad X^*_{\mathcal{A}} \leftarrow$ MUTATE$(X^*_{\mathcal{A}}, \mathcal{S}, l_{target}, M)$
14: $\quad\quad\quad$**if** **IsADI**$(X^*_{\mathcal{A}}, \mathcal{S}, l_{target}, M) == true$ **then**
15: $\quad\quad\quad\quad$add $(X^*_{\mathcal{A}}, l_{target})$ in $\mathcal{O}$
16: $\quad\quad\quad$**else if** REDUCESALIENCY$(X^*_{\mathcal{A}}, l_{target}, M) == true$ **then**
17: $\quad\quad\quad\quad$add $(X^*_{\mathcal{A}}, l_{target})$ in $\mathcal{Q}$
18: $\quad$**return** ADI Set $\mathcal{O}$

to $\mathcal{B}$. However, for ethical users and developers, $\mathcal{S}$ cannot be collected in the same way, as sharing user data may compromise privacy even if $\mathcal{S}$ is minimal.

This section designs greybox fuzzing to uncover ADIs for VFL vulnerability assessment without using $\mathcal{S}$ but under the collaboration with $\mathcal{B}$. Many studies have examined using testing to find inputs that can manipulate DNN predictions [75, 100]. Nonetheless, we investigate a novel design point — *efficient and privacy-preserving fuzz testing in VFL.*

A. Design of Greybox Fuzz Testing

Greybox software fuzzing is an evolutionary process in which inputs that reveal new code coverage are retained for more mutations until vulnerabilities are detected. In VFL, we consider an input $X^*_{\mathcal{A}}$ of participant $\mathcal{A}$ interesting if $X^*_{\mathcal{A}}$ reduces contribution of other participants to the joint prediction. Although the "contribution" can be revealed using saliency scores, VFL systems do not allow such disclosure.

Inspired by our gradient-based ADI synthesis approach (Sec. IV), we extend the standard VFL systems by allowing participants to compute and share saliency scores to guide greybox fuzzing; the shared saliency score serves the feedback for fuzzing, which is comparable to how code coverage is used to guide software fuzzing [105]. We assume that:

> Although sharing saliency may raise potential concerns of privacy violation, to assess ADI attack vectors before security breaches, normal participants should have enough incentive to collaborate and share saliency scores.

Again, this stage allows VFL developers to launch **in-house vulnerability assessment by comprehensively uncovering ADIs**. The saliency score is derived from the the saliency map's l_1 norm, which has *limited sensitivity*. Privacy leakage due to saliency score, though theoretically possible, is low in practice. More importantly, with over two participants, secure aggregators may be used to shield each participant's saliency score and increase privacy [16, 19].

Alg. 2 depicts the high-level procedure of our feedback-driven fuzzing. We clarify full implementation details of cooperating fuzzing with VFL in Appx. K. **FUZZING** is the entry point, where **ISADI** checks whether a given input $X^*_{\mathcal{A}}$ of $\mathcal{A}$ can dominate other participants $\mathcal{B}$'s contributions. **ISADI** allocates a set to collect all joint inference outputs (line 2). It then iterates all inputs $X^i_{\mathcal{B}} \in \mathcal{S}$ used by $\mathcal{B}$ and records each joint inference output o (lines 4–5). STABLE checks whether outputs in $\mathcal{T}$ are identical to its target label l_{target}.

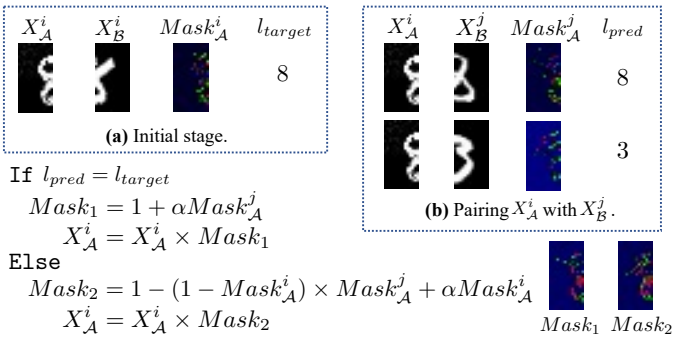


Fig. 5: Saliency-aware mutation.

FUZZING accepts a corpus of seeds $\mathcal{C}$ to initialize queue $\mathcal{Q}$ (line 8). This function also takes in the jointly trained model M and $\mathcal{S}$. For fuzzing, inputs in $\mathcal{S}$ are *hidden* from $\mathcal{A}$. Rather, $\mathcal{B}$ uses inputs in $\mathcal{S}$ to cooperate with $\mathcal{A}$ and facilitate **ISADI** and MUTATE (line 13 in Alg. 2). We use $\mathcal{O}$ to store identified ADIs (line 8). The entire campaign is subjected to *MAX_ITER* iterations, and for each iteration, we pick one input $X^*_{\mathcal{A}}$ and its target label l_{target} by popping $\mathcal{Q}$ (line 10) and determine #mutation by function ASSIGNENERGY over $X^*_{\mathcal{A}}$ (line 11). *MAX_ITER* is currently 5,000, and each $X^*_{\mathcal{A}}$ has a fixed "energy" of ASSIGNENERGY$(X^*_{\mathcal{A}}) = 20$.

During each iteration, we generate a new variant $X^*_{\mathcal{A}}$ by mutating the original $X^*_{\mathcal{A}}$ (line 13). When ADIs are found (line 14), we add the input $X^*_{\mathcal{A}}$ into $\mathcal{O}$. $X^*_{\mathcal{A}}$ is "interesting" by successfully reducing the saliency of $\mathcal{B}$; we thus add $X^*_{\mathcal{A}}$ to the queue for further mutations (lines 16–17). Alg. 2 will return all uncovered ADIs for users to assess security and attack interface of their VFL systems (line 18).

Design REDUCESALIENCY (Line 16). We decide whether input $X^*_{\mathcal{A}}$ of $\mathcal{A}$ is prone to becoming an ADI by assessing its influence on $\mathcal{B}$, which is modeled using the saliency scores of $\mathcal{B}$. As previously discussed, we assume that the saliency score is faithfully shared by $\mathcal{B}$. Software greybox fuzzing [105] looks for inputs that achieve new code coverage. Similarly, REDUCESALIENCY checks whether $X^*_{\mathcal{A}}$ can successfully *decrease* the saliency scores shared by $\mathcal{B}$. This way, we identify and retain $X^*_{\mathcal{A}}$ to gradually minimize $\mathcal{B}$'s contribution. Saliency scores are computed using **SALIENCY_EST** presented in Alg. 1. Each saliency score, a float number ranging from 0 to 1, is derived from the saliency map's l_1 norm. A lower saliency score implies that $\mathcal{B}$ contributes less to joint inference. The saliency score is more coarse-grained than the saliency map. It may not be inaccurate to assume that saliency scores disclose only limited information regarding inputs of $\mathcal{B}$, pragmatically alleviating privacy leakage concerns.

TABLE II: Evaluation setup over VFL participants $\mathcal{A}$ and $\mathcal{B}$.

Dataset	#Cases	Learning Protocol	Participant $\mathcal{A}$		Participant $\mathcal{B}$		Central Coordinator $\mathcal{C}$
			#Partitioned Features	Setup	#Partitioned Features	Setup	
NUS-WIDE	269,648	SplitNN	634	2-FCs with ReLU	1,000	2-FCs with ReLU	2-FCs with ReLU
Credit	30,000	HeteroLR	13	1-FC	10	1-FC	Sigmoid
Vehicle	946	HeteroLR	9	1-FC	9	1-FC	Sigmoid
MNIST	60,000	SplitNN	28×14 pixels	3-Convs with ReLU	28×14 pixels	3-Convs with ReLU	1-FC with ReLU
VQA v2.0	82,783	VFVQA	embedding to 50×2054	FasterRCNN [79]	embedding to 128×512	BERT [56]	Multi-Layer Transformers
CIFAR-10	50,000	SplitNN	embedding to 10752	VGG16 [83]	embedding to 10752	VGG16 [83]	3-FCs with ReLU

Saliency-Aware Mutation (Line 13). We propose a saliency-aware scheme to mutate inputs. Fig. 5 illustrates the mutation procedure using MNIST images as an example. As will be introduced in Sec. VII, each MNIST image is vertically partitioned into two pieces in a VFL setting. Given a pair of input $X^i_{\mathcal{A}}$ and $X^i_{\mathcal{B}}$ belonging to the same MNIST image i, we first compute the saliency map of $X^i_{\mathcal{A}}$ as $Mask^i_{\mathcal{A}}$ and the jointly inferred label l_{target} (Fig. 5(a)).

We mutate $X^i_{\mathcal{A}}$ with some random noise, and then iterate inputs in $\mathcal{S}$. For an input pair $X^i_{\mathcal{A}}$ and $X^j_{\mathcal{B}}$ ($j \neq i$), we compute a new saliency map $Mask^j_{\mathcal{A}}$ (Fig. 5(b)). When the joint inference l_{pred} equals l_{target}, we retain this mutation by augmenting $X^i_{\mathcal{A}}$ with $\alpha Mask^j_{\mathcal{A}}$ (`If` branch in Fig. 5(c)). $l_{pred} \neq l_{target}$ denotes undesirable mutations (`Else` branch in Fig. 5(c)): we weaken certain pixels in $X^i_{\mathcal{A}}$ in case they are focused by $Mask^j_{\mathcal{A}}$ but overlooked by $Mask^i_{\mathcal{A}}$. α is empirically decided as 0.2. Intuitively, selecting a proper α is conceptually similar to selecting a "learning rate", a common step in training neural networks. For a smaller α, we expect more mutation energy to converge and discover an ADI; for a larger α, we may miss the targeted point. Our preliminary exploration shows that $\alpha = 0.2$ and 20 energy denote reasonably good configurations. $Mask^{i,j}_{\mathcal{A}}$ is calculated using the algorithm in [34], where the saliency mask is a matrix with values ranging from 0 to 1. To boost a participant p's contribution, according to [34], we can increase certain input components of p that correlate to large values on p's saliency mask.

We repeat this procedure over $\mathcal{S}$ to update $X^i_{\mathcal{A}}$. We use *bounded mutation* over $X^i_{\mathcal{A}}$ to retain stealthy changes. The proposed mutation has a time complexity linear to $|\mathcal{S}|$. As $|\mathcal{S}|$ is tiny (e.g., 20 for our evaluation in Sec. VII-B), time complexity is not a major issue. Furthermore, our saliency-aware mutation is a general pipeline agnostic to input formats; it performs more holistic and efficient mutations than pixel-level mutations. Sec. VII-B shows that a large number of ADIs are uncovered across all datasets using fuzz testing.

VI. Implementation & Evaluation Setup

VFL Protocols & Frameworks. As discussed in Sec. II, HeteroLR and SplitNN are two popular and core VFL protocols that can be extended to most parameterized VFL protocols (e.g., VFVQA). Hence, we evaluated these two protocols; see implementation and training details in Appx. I. To implement VFVQA, we modify the state-of-the-art VQA model Oscar [56] into VFL. In VQA, one participant raises natural-language questions about images possessed by the other participant. VFVQA allows two participants to conduct VQA while keeping questions/images locally; see Appx. I for VFVQA architecture and implementation details. To date, several VFL infrastructures are available, including FATE [8], TF Federated [5], FedML [47], PySyft [3], and CrypTen [2]. We choose FATE and FedML due to their popularity and support for common VFL protocols including HeteroLR and SplitNN. FATE is maintained by industry, whereas FedML is a state-of-the-art VFL framework developed by the research community and industry. Both platforms are in high engineering quality. Our main findings are, to our knowledge, independent to VFL frameworks. We use the default SplitNN implementation in FATE, and extend the HeteroLR implementation in FedML.

VII. Evaluation

Datasets & Environment Setup. We use six popular real-world datasets: NUS-WIDE [25], Credit [1], Vehicle [6], MNIST [52], VQA v2.0 [57], and CIFAR-10 [51]. Each dataset's features are partitioned between VFL participants $\mathcal{A}$ and $\mathcal{B}$, as in Table II. For NUS-WIDE, $\mathcal{A}$ holds the image features and $\mathcal{B}$ holds the text features. For Credit, $\mathcal{A}$ holds 13 features and $\mathcal{B}$ holds 10. For Vehicle, both $\mathcal{A}$ and $\mathcal{B}$ get nine features. For MNIST, each image is vertically partitioned into two: $\mathcal{A}$ gets the left piece (with 28×14 pixels) and $\mathcal{B}$ gets the right. For VQA v2.0, $\mathcal{A}$ holds images and $\mathcal{B}$ raises natural-language questions. For CIFAR-10, $\mathcal{A}$ and $\mathcal{B}$ each holds a $10,752$-dimensional feature embedding, which is the feature output of VGG16 with the left and right piece of the image as the inputs. We summarize the setup in Table II, and present details of dataset preparation and setup in Appx. L. Our evaluation is conducted on Intel Xeon CPU E5-2683 with 256 GB RAM and Nvidia GeForce RTX 2080 GPU.

Metrics. We measure the performance of our attack using *success rates* and *average dominated proportion of $\mathcal{B}$'s inputs*. Recall as we defined in Def. 2, to decide if an input $X^i_{\mathcal{A}}$ is ADI, we check if $X^i_{\mathcal{A}}$ can dominate more than a threshold of all test inputs of $\mathcal{B}$. As defined in Sec. III, we adopt two thresholds (95% and 99%) as a practical assessment of ADIs. Accordingly, we define the ratio of samples from $\mathcal{A}$'s test dataset that can be successfully perturbed into ADIs as the attack "success rate" of ADI synthesis. We also measure the average dominated proportion of $\mathcal{B}$'s inputs. That is, for a generated input on $\mathcal{A}$, we measure how much of the benign participants' data is dominated. For simplicity, we refer to this metric as ADP in the paper. The ADP is the average of r over the generated data $X^*_{\mathcal{A}}$ (r is the dominated proportion of $\mathcal{B}$'s inputs for a single input from $\mathcal{A}$ as noted in Def. 2).

Dominating Inputs in Standard Datasets. We first assess the input dominating issues (without perturbation) in $\mathcal{A}$'s

TABLE III: Dominating rates of the standard datasets.

	Dominating Rate		ADP	Model Accuracy on Test Datasets
	95%	99%		
NUS-WIDE	0.00%	0.00%	38.93%	77.35%
Credit	25.0%	2.10%	82.40%	0.7450 (auc-roc)
Vehicle	0.86%	0.14%	40.74%	84.00%
MNIST	0.87%	0.20%	47.54%	97.78%
VQA v2.0	NA	0.80%	38.84%	73.82%
CIFAR-10	2.63%	0.46%	46.40%	86.55%

standard datasets. Using the aforementioned feature partition scheme, we train VFL models for two participants $\mathcal{A}$ and $\mathcal{B}$. Table III's last column shows that each trained model has achieved satisfying accuracy. Table III reports the dominating rates, i.e. the ratio of standard inputs of $\mathcal{A}$ that dominate the VFL predictions. Such standard inputs of $\mathcal{A}$ are deemed as ADIs. Recall when deciding if an input is ADI, our practical assessment (Def. 2) examines two thresholds, 95%, and 99%. The outlier is VQA v2.0, where an image is regarded as an ADI only when it dominates *all* of its associated questions (typically one image associated with 3–10 questions). Hence, the threshold should be 100.0% rather than 95% or 99% when assessing its input dominating issues. To ease presentation, for Table III and the rest tables, we put the VQA v2.0 evaluation results in the 99% column and "NA" in the 95% column. We also report the ADPs for standard inputs from $\mathcal{A}$ in the third column of Table III.

Credit has a greater dominating rate at 95%, and its ADP is higher than others. Credit is a binary classification task with a small sample size, and it is likely to identify "dominating inputs" (i.e., false positives) of $\mathcal{A}$ which induce identical outputs when paired with $\mathcal{B}$'s inputs. To eliminate false positives, saliency maps of $\mathcal{B}$'s inputs can be used to confirm if its contribution is negligible. Overall, we interpret that dominating inputs are rare in well-designed/trained models with a fair feature partition. Without an active adversary, users are unlikely to notice ADIs until a security breach. However, when feature partition over two participants is unbalanced, ADIs become noticeable; see Appx. F.

Setup. In the following, we will first evaluate the performance of our proposed ADI synthesis in Sec. VII-A. Note that in addition to launching the blackbox attack, we also set up a whitebox synthesis, where $\mathcal{A}$ is assumed to acquire gradients from $\mathcal{B}$'s model. This is aligned with our formulation of whitebox synthesis in Alg. 1. To clarify, this work champions blackbox VFL attacks. We set up the whitebox synthesis simply as a **baseline** for comparison with the blackbox attack. In Sec. VII-A, we also analyze the properties of ADIs like the stealthiness and the reward hogging. Then, we evaluate the greybox fuzz testing in Sec. VII-B and present the empirical comparison between ADIs, AEs and random inputs in Sec. VII-C. We then evaluate the performance of two defense strategies in Sec. VII-D. In Sec. VII-E, we explore the feasibility of synthesizing ADIs without accessing the data of $\mathcal{B}$. In addition, we also evaluate several key factors in our attack like size of $\mathcal{S}$ (Appx. D), feature partition ratio (Appx. F), and number of participants (Appx. G).

A. Gradient-Based ADI Synthesis

Results. Table IV reports the success rates of ADI synthesis under different settings, thresholds, and mutation strategies in whitebox and blackbox settings. Complex datasets and models like NUS-WIDE, MNIST, VQA v2.0, and CIFAR-10 have a lower success rate than simple datasets like Credit and Vehicle, especially when the threshold is 99%. For Credit and Vehicle, the success rate is close to 100% under random mutation. We also observe that for CIFAR-10, it is relatively easy to achieve high attack success rate under the 95% threshold. Recall we split CIFAR-10 images to two pieces. Given CIFAR-10 images are generally complex, it is inherently hard for the model to capture meaningful contents using just one split. Hence, it becomes easier to dominate benign participants. In contrast, the MNIST hand-written digits are easier, making it possible for the model to extract useful information even with only one image split. This explains that for MNIST, generating ADIs are less easy. Under the 99% threshold, it is generally harder to generate ADIs for the CIFAR-10 and MNIST setups compared to the simple datasets like Credit and Vehicle.

The bounded mutation scheme confines the applied mutations to a practical range (i.e., bounded by the variance of the mutated feature). We find that this scheme still achieves plausible success rates of over 50% for simple tasks like Credit and Vehicle and over 35% for complex tasks under the 95% threshold. 99% threshold is more challenging, and therefore, the success rate becomes reasonably lower. In Table V, we report the ADP. Considering our ADI definition (Def. 2), it is trivial that the ADP must be higher than 95% or 99%, when benchmarking with ADIs found under the 95% or 99% thresholds. More importantly, the last column of Table V reports the ADPs of all generated inputs (though some of them are not "ADIs"). The ADPs are consistently higher across all settings, compared to the standard datasets (Table III). This further demonstrates the effectiveness of our ADI synthesis algorithm as the generated inputs tend to dominate the other participants' inputs.

In compared to whitebox synthesis, the blackbox synthesis has decreased success rates, as shown in Table IV. This is reasonable, given the difficulty and unreliability of estimating gradients using FDM. Overall, the success rates of blackbox and whitebox syntheses have similar trending, with complex datasets like NUS-WIDE having a lower success rate than simple datasets. We also find that for the bounded mutation (99%) evaluation over NUS-WIDE, the success rates of the blackbox attack is increased. In comparison to simple datasets, the NUS-WIDE dataset has larger feature dimensions and a denser and more complicated feature distribution. All these factors contribute to the difficulty of solving the optimization problem in whitebox synthesis (line 12 in Alg. 1). Also, the estimated gradients in the blackbox setting may be a bit larger than the real gradients, which will speed up convergence to some extent. Thus, the blackbox ADI synthesis using bounded mutation under the 99% threshold has a slightly higher success rate. In sum, the evaluation illustrates that ADIs can be

TABLE IV: Success rates of gradient-based ADI synthesis.

	Dataset	Random Mutation		Bounded Mutation	
		95%	99%	95%	99%
Whitebox	NUS-WIDE	65.1%	49.6%	42.8%	22.0%
	Credit	99.8%	99.6%	87.6%	52.6%
	Vehicle	98.4%	97.0%	87.9%	74.8%
	MNIST	92.9%	62.5%	34.5%	16.7%
	VQA v2.0	NA	47.4%	NA	14.2%
	CIFAR-10	99.6%	53.4%	98.9%	44.3%
Blackbox	NUS-WIDE	45.2%	35.6%	40.0%	32.8%
	Credit	99.0%	98.3%	54.1%	41.1%
	Vehicle	96.4%	76.2%	87.1%	60.0%
	MNIST	78.8%	51.9%	33.9%	4.85%
	VQA v2.0	NA	41.5%	NA	10.9%
	CIFAR-10	97.7%	52.7%	91.3%	43.8%

TABLE V: ADPs of gradient-based ADI synthesis.

	Dataset	Random Mutation			Bounded Mutation		
		95%	99%	All	95%	99%	All
Whitebox	NUS-WIDE	99.87%	99.93%	78.06%	99.43%	99.85%	75.44%
	Credit	99.79%	99.81%	98.99%	99.20%	99.82%	93.88%
	Vehicle	99.75%	99.92%	87.02%	99.52%	99.71%	85.13%
	MNIST	98.21%	99.79%	98.38%	97.41%	99.79%	90.91%
	VQA v2.0	NA	100%	61.97%	NA	100%	50.40%
	CIFAR-10	98.65%	99.50%	98.64%	98.51%	99.46%	98.45%
Blackbox	NUS-WIDE	99.15%	99.80%	75.35%	99.13%	99.84%	73.30%
	Credit	99.81%	99.83%	99.10%	99.22%	99.80%	93.86%
	Vehicle	99.01%	99.98%	87.09%	99.34%	99.98%	83.14%
	MNIST	98.22%	99.55%	93.43%	97.90%	99.18%	85.82%
	VQA v2.0	NA	100%	67.96%	NA	100%	63.72%
	CIFAR-10	98.67%	99.49%	97.00%	98.62%	99.36%	98.15%

synthesized practically in blackbox settings, despite variances in the datasets, VFL protocols, and mutation strategies. We envision that VFL systems are in high risk of being controlled by ADIs.

ADI Stealth. ADIs generated by bounded mutation mostly follow the original datasets' distribution, making them visually similar to normal inputs. In Fig. 6, we project original inputs and ADIs synthesized at threshold 99% to 2D figures using multidimensional scaling. We interpret that ADIs generated by bounded mutation (marked in red) can neither be easily distinguished by the data distribution nor by the distances between the data points. Note that since the data has multiple dimensions, the 2-dimensional projection figure may not reflect the real distribution distance. To mitigate this threat to validity, we run the multidimensional scaling for multiple times and confirm that the results are consistent. Fig. 7 reports stealthy ADIs synthesized by bounded mutation. While perturbing the left half of MNIST images (the first column of Fig. 7) only causes stealthy changes (the second column of Fig. 7), the synthesized ADIs, after concatenating with the right half of arbitrary MNIST images (i.e., the inputs of $\mathcal{B}$; see the third column of Fig. 7), control the outputs to fixed labels (the last column of Fig. 7).

Moreover, we also train a binary classifier using the same amount of ADIs and normal inputs to distinguish them. It only achieves 0.54 ROC-AUC, which is very close to random guessing. Thus, we conclude that ADIs generated by bounded mutation and the normal inputs are hard to distinguish, which empirically illustrates the stealth of ADIs.

Fig. 8 shows intriguing cases from MNIST dataset. As shown in the "Concatenation/Expectation" column of Fig. 8, while ADIs may form reasonable digits (from a human perspective) with the inputs of $\mathcal{B}$, the joint inferences are still forced to be the target labels specified by the adversary. We also provide the saliency maps associated with the input images, which imply that the contribution of $\mathcal{B}$ is negligible (the saliency maps in the 4th column barely have highlighted areas). This again shows that ADIs can govern the joint inference and negate other participants' contributions.

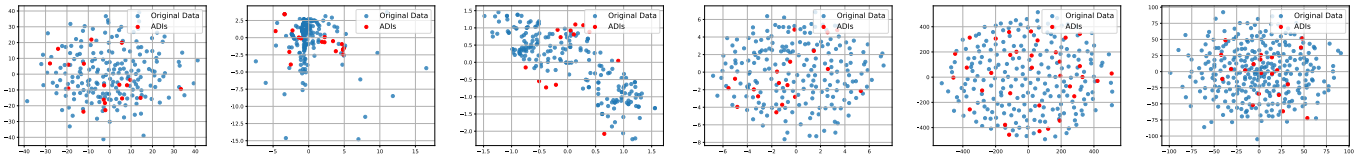
Whether concatenating ADIs and normal inputs can form meaningful contents depend on the nature of features that VFL participants hold. For instance, in MNIST, the features hold by different participants are images. Therefore, forming "meaningful concatenations" requires that both adversarial and benign participants provide *visually-correlated* images. This is apparently challenging, though many successful cases (as in Fig. 8) are found in our evaluation. In contrast, datasets like Credit consist of low-dimensional numeric vectors; "visual correlation" is not a concern for such numeric data. It is generally easier for concatenations of ADIs and benign participant's inputs to be indistinguishable with normal data in Credit. Though it is not the primary focus of this research, we deem it interesting to explore synthesizing ADIs that can form meaningful concatenations with benign participants' inputs. The challenge is to quantify the distinguishability between the concatenations and normal inputs to define an objective function.

Reward Estimation under ADIs. Sec. II and Sec. III-A have discussed that FL clients are often compensated based on their contributions to the joint inference. While the evaluated VFL frameworks do not ship with a reward calculation module, we estimate how ADIs influence reward allocation in Appx. E. As expected, while $\mathcal{A}$ and $\mathcal{B}$ earn roughly the same reward when using normal inputs, ADIs allow adversary $\mathcal{A}$ to hog rewards for each inference. We deem this evaluation as convincing to show that ADIs can create real-world financial loss and confusion for normal consumers.

B. Greybox Fuzz Testing

Fuzz testing helps in-house VFL vulnerability assessment. As mentioned in Sec. V-A, we use bounded mutation to mutate inputs: bounded mutation generates more realistic inputs, which assesses VFL in front of stealthy ADIs.

Table VI reports the fuzzing results. For datasets with narrow feature spaces (Credit and Vehicle), we use 500 seeds and finish in two hours. For others, we run a 12-hour campaign with a corpus of 1,000 seeds to systematically explore the input spaces. ADIs are found in similar numbers for all settings, indicating high efficiency of the proposed technique across input formats and VFL protocols. Recall that the fuzzing algorithm has relatively high time complexity; our saliency-aware mutation (line 13 in Alg. 2) and **IsADI** function (line 1 in Alg. 2) both require iterating all inputs in $\mathcal{S}$ for each fuzzing iteration. Nevertheless, our results in Table VI show that a high number of ADIs can be found in a half-day even for image inputs. We interpret the performance as plausible: fuzzing allows developers to quickly assess the ADI risk of their VFL at a low cost.



(a) NUS-WIDE. (b) Credit. (c) Vehicle. (d) MNIST. (e) VQA v2.0. (f) CIFAR-10.

Fig. 6: Normal inputs and ADIs projected to 2D figures.

TABLE VI: Fuzz testing results.

	#ADIs		#Seeds	Processing
	95%	99%	in Corpus	Time
NUS-WIDE	176	98	1,000	12 hours
Credit	235	136	500	2 hours
Vehicle	392	157	500	2 hours
MNIST	113	86	1,000	12 hours
VQA v2.0	NA	93	1,000	12 hours
CIFAR-10	773	61	1,000	12 hours

TABLE VII: Comparing ADIs and AEs.

	ADP			Success Rate (95% threshold)		
	ADI	AE	Random Inputs	ADI	AE	Random Inputs
NUS-WIDE	75.44%	33.15%	43.25%	42.8%	0.00%	0.00%
Credit	93.88%	83.98%	89.21%	87.6%	13.0%	52.7%
Vehicle	85.13%	46.45%	56.16%	74.8%	2.84%	10.5%
MNIST	90.91%	42.67%	31.90%	34.5%	0.20%	0.00%
VQA v2.0	50.54%	3.91%	19.15%	14.2%	2.80%	0.60%
CIFAR-10	98.45%	43.55%	16.52%	98.9%	1.78%	0.00%

TABLE VIII: Detector performance.

	95% Threshold		99% Threshold	
	Avg. Acc	Avg. F1	Avg. Acc	Avg. F1
NUS-WIDE	74.25%	62.24%	81.76%	77.18%
Credit	72.41%	59.96%	77.14%	67.22%
Vehicle	85.09%	79.13%	89.47%	85.92%
MNIST	64.16%	52.99%	76.03%	63.78%
VQA v2.0	NA	NA	56.52%	40.24%
CIFAR-10	60.40%	32.67%	67.53%	53.79%

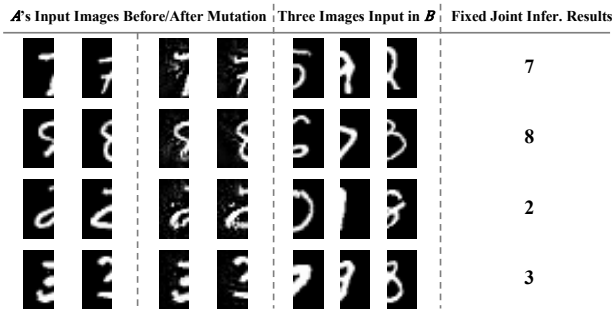


Fig. 7: ADIs found in MNIST using bounded mutation.

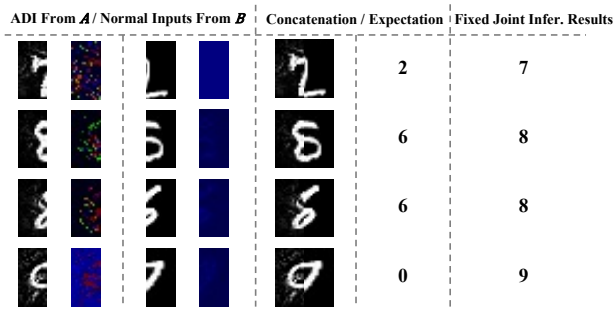


Fig. 8: ADIs dominating the joint inference even when the concatenated images form reasonable digits.

Stealth of ADIs. We compare ADIs with normal inputs following the same procedure of reporting Fig. 6; the results are in Appx. M. We find that ADIs are highly similar to regular inputs. We also present ADIs found by fuzzing and their saliency maps in Appx. M. Findings (i.e., ADIs greatly reduce the contribution of normal inputs) are consistent with Fig. 8.

C. Comparing ADIs and Standard AEs

Following Sec. III which compares ADIs and AEs from the conceptual level, we now empirically compare them. We first generate AEs in the VFL setting using a classic AE generation algorithm, FGSM [40]. We then measure the number of AEs, when being used as inputs of $\mathcal{A}$, that can dominate over 95% normal inputs from $\mathcal{B}$. Similar to Table IV, we also report the ADP. As a comparison, besides AEs, we set up the same evaluation using randomly-generated inputs and using ADIs we generated in Sec. VII-A. The random inputs are uniformly sampled from the feature space of $\mathcal{A}$'s normal inputs. The results are shown in Table VII.

As expected, the ADPs in the AE evaluation are much lower than that of ADIs, and are comparable to the randomly-generated inputs. Similar observations are made for the attack success rate evaluations as well. For instance, the average ADPs across different datasets are 82.39% for ADIs, 42.29% for AEs, and 42.70% for randomly-generated inputs. Similarly, the average attack success rates across different datasets are 58.79% for ADIs, 3.44% for AEs, and 10.63% for randomly-generated inputs.

The results further demonstrate the effectiveness of ADIs. As explained in Sec. III-A, each AE aims to manipulate one specific input of $\mathcal{B}$, and it is agnostic to other inputs from $\mathcal{B}$. Also, AE synthesis does not explicitly consider diminishing the contribution of $\mathcal{B}$. In contrast, ADI synthesis aims to find an input that can dominate the model output and control the majority of $\mathcal{B}$'s inputs. Moreover, ADIs explicitly minimize the contribution of the benign participants. In sum, findings in Table VII empirically illustrates the distinction between AEs and ADIs; we conclude that AEs and randomly-sampled inputs are much less effective in dominating the outputs of the VFL system compared with ADIs.

D. Mitigating ADIs with Two Defense Schemes

In this section, we explore the effectiveness of two common defense methods against AEs: clustering-based detector and adversarial training. Clustering-based detector is commonly used to detect the out-of-distribution data, and it has been widely-used in mitigating conventional AEs [13, 87]. We use ADIs generated in Sec. VII-A (using gradient-based whitebox synthesis) and collect the local model outputs when processing these ADIs. We then randomly select the same number of normal inputs from $\mathcal{A}$'s test dataset and collect the corresponding local model outputs. We further run the K-means clustering algorithm [65] to cluster the outputs into K clusters, and we mark ADI clusters and normal clusters according to the proportion of ADI outputs and normal data outputs in each

TABLE IX: Adversarial training results.

	Accuracy on Test Dataset	Accuracy on AE Dataset	Attack Success Rate	
			95%	99%
NUS-WIDE	73.13%	64.06%	34.9%	16.4%
Credit	0.7347 (auc-roc)	77.40%	96.0%	40.8%
Vehicle	84.00%	80.00%	89.6%	87.7%
MNIST	97.93%	90.46%	33.4%	13.8%
CIFAR-10	85.97%	66.97%	97.9%	27.8%

TABLE X: Blackbox bounded mutation without $\mathcal{S}$.

	Attack Success Rate		ADP		
	95%	99%	95%	99%	All
NUS-WIDE	14.9%	11.3%	99.14%	99.90%	66.50%
Credit	54.0%	41.2%	99.20%	99.81%	93.88%
Vehicle	57.2%	56.2%	99.94%	99.98%	80.81%
MNIST	15.5%	1.45%	96.81%	99.01%	78.37%
VQA v2.0	NA	21.4%	NA	100%	53.95%
CIFAR-10	69.3%	52.2%	99.18%	99.70%	80.89%

cluster. In practice, we found that $K = 5$ is a good option for our datasets, because on average, we have a few hundreds data samples for each clustering task. Users may also generate more ADIs using our fuzz testing-based ADI discover algorithm.

We repeat the clustering procedure for ten times and report the average detection accuracy and the average F1 scores in Table VIII. The F1 score is defined as $F1 = \frac{2*precision*recall}{precision+recall} \in [0, 1]$. A higher F1 score indicates better performance. The results show that our clustering-based detection method is reasonably effective but cannot reach very high accuracy. We achieve over 60% accuracy and over 50% F1 score for most datasets. Due to the complexity of the task and the size of the feature space, detectors in the VQA v2.0 and CIFAR-10 evaluations are less effective. Also, detectors under 99% threshold are generally more accurate than the 95% case. Overall, we find that to generate ADIs under 99% threshold, more mutations are generally needed, and therefore, the ADIs often become more distinguishable under 99% threshold.

Overall, we deem the detection as effective, and it is a promising and demanding direction to improve detection accuracy further. We also emphasize that the clustering algorithm uses local model outputs instead of the raw inputs. Thus, the results are not contradictory to the stealthiness evaluation of ADIs. Moreover, the benign participant needs to access the intermediate outputs of the adversarial participants, and need to know in advance whether the outputs are generated by ADIs or normal inputs to tune the detector. Thus, deploying the mitigation is challenging and under development, especially when there is no trusted coordinator in VFL systems.

In addition, we also evaluate the gradient-based ADI synthesis under the adversarial training defense that is designed to mitigate standard AEs. We use adversarial training techniques from [91] to train robust models, and then generate ADIs on the robust models using gradient-based ADI synthesis. The setting is the same as Sec. VII-A. The results presented in Table IX show that the accuracy of the trained robust models on the test datasets are close to the non-robust models in Table III. And the accuracy on the AE datasets are high, i.e., all of the robust models achieve around or higher than 65% accuracy. To compare, the non-robust models' accuracy on the AE datasets is lower than 30%. Also, for the VQA task, it is non-trivial to perform adversarial training on the large models like BERT [30]. Thus, we omit the results for VQA v2.0 in Table IX. Given that said, we view our findings as convincing, which illustrate that adversarial training is not effective to mitigate ADIs.

Moreover, the ADI attack success rates are comparable to that of the non-robust models, whose results are in Table IV (the "whitebox" setting). We therefore conclude that the adversarial training methods that designed for mitigating AEs are not effective in mitigating ADIs. As we have discussed in Sec. III and Sec. VII-C, the objectives of ADIs and AEs are distinct, and evaluations here show that the AE defense methods cannot be generalized to mitigate ADIs.

E. Attack without Accessing $\mathcal{S}$

This section assesses gradient-based ADI synthesis when $\mathcal{A}$ cannot access the dataset $\mathcal{S}$ of $\mathcal{B}$. $\mathcal{A}$ only knows the range of $\mathcal{B}$'s input data. Aligned with settings in previous sections, we randomly generate 20 $\mathcal{B}$'s inputs. The generated inputs are uniformly distributed in $\mathcal{B}$'s feature ranges.

We conduct the experiments on the blackbox setting with bounded mutation strategy, and the settings are the same as Sec. VII-A. The results in Table X show that the ADI synthesis algorithm can effectively generate ADIs. The attack success rates and the ADPs are reasonably high compared to the results when $\mathcal{A}$ can access $\mathcal{S}$. For instance, we achieve 15.5% attack success rate under the 95% dominating threshold on MNIST and the ADP is 78.37%. Recall the results, when $\mathcal{A}$ can access $\mathcal{S}$, are 33.9% and 85.82%, respectively (shown in Table IV and Table V). The observations are similar on other datasets. In sum, evaluations show that non-trivial amount of ADIs can be generated, even though $\mathcal{A}$ does not have access to $\mathcal{B}$'s data. The results further emphasize the feasibility of performing ADI attacks on real-world VFL systems.

VIII. Discussion

ADI Mitigation with Fine-Tuning. We have evaluated the clustering-based ADI detector and adversarial training techniques in Sec. VII-D. However, they cannot achieve high accuracy to form a practical solution to mitigate ADIs.

Careful readers might ask if the fine-tuning techniques using the generated ADIs as training data can improve the robustness of the model to defense against ADIs. At this step, we launch a tentative experiment to fine-tune the model with the generated ADIs using bounded mutation under the 95% threshold on MNIST and CIFAR-10. The accuracy of the MNIST model increases by 0.04%, and the accuracy of the CIFAR-10 model decreases by 0.62%. And we successfully mitigate 64.2% and 94.0% of MNIST and CIFAR-10 ADIs. That is, after fine-tuning, only 35.8% and 6.0% of the previously found ADIs still achieve a dominating rate higher than 95%, and we do not sacrifice much of the model's performance on the test dataset. Given that said, we believe it is hard to completely eliminate future generation of ADIs on the fine-tuned model, as long as the participants are making nontrivial contributions to the model prediction. Holistically, fine-tuning fixes some known ADIs on hand by boosting the contribution of benign

parties (to "un-dominate" adversarial participants who use ADIs). But this sheds light on a concern, such that when those benign parties are exploited and become "adversarial" in the future, they are powerful enough to easily dominate other parties with ADIs. In sum, with findings in Sec. VII-D and explorations here, we see it as demanding (and technically challenging) to propose specific ADI detection and mitigation techniques with high accuracy; we leave it as one future work. Furthermore, we anticipate to leverage fuzzing-based ADI discovery algorithm to continously gather ADIs and fine-tune VFL systems. We foresee a stage when the fuzzing process can hardly find sufficient ADIs, indicating that the continuously-tuned VFL systems have acquired a high level of robustness. We provide further discussions on attacking tree-based models and selection of $\mathcal{S}$ in Appx. C.

IX. Conclusion

This paper exploits VFL using ADIs. ADIs control the joint inference and diminish benign clients' contribution. We first prove that ADIs exist in common VFL. We then propose both gradient-based ADI synthesis and fuzz testing for developers to perform in-house vulnerability assessment. We assess the impact of various settings on ADI generation. Our study exposes novel VFL attack vectors, promoting early detection of unknown threats and more secure VFL.

Acknowledgment

We thank anonymous reviewers for their valuable feedback. The HKUST authors were supported in part by the research fund provided by HSBC.

References

[1] Credit Dataset. https://archive.ics.uci.edu/ml/datasets/default+of+credit+card+clients.
[2] CrypTen. https://github.com/facebookresearch/CrypTen.
[3] PySyft. https://github.com/OpenMined/PySyft.
[4] Research artifact. https://github.com/Qi-Pang/ADI.
[5] TensorFlow Federated: Machine Learning on Decentralized Data. https://www.tensorflow.org/federated.
[6] Vehicle. https://archive.ics.uci.edu/ml/datasets/Statlog+(Vehicle+Silhouettes).
[7] Visual Question Answering in the Medical Domain. https://www.imageclef.org/2020/medical/vqa.
[8] FATE: An industrial grade federated learning framework. www.fedai.org, 2020.
[9] Elie Alhajjar, Paul Maxwell, and Nathaniel Bastian. Adversarial machine learning in network intrusion detection systems. *Expert Systems with Applications*, 186:115782, 2021.
[10] Stanislaw Antol, Aishwarya Agrawal, Jiasen Lu, Margaret Mitchell, Dhruv Batra, C. Lawrence Zitnick, and Devi Parikh. VQA: Visual Question Answering. ICCV, 2015.
[11] Anish Athalye, Logan Engstrom, Andrew Ilyas, and Kevin Kwok. Synthesizing robust adversarial examples. ICML, 2018.
[12] Eugene Bagdasaryan, Andreas Veit, Yiqing Hua, Deborah Estrin, and Vitaly Shmatikov. How to backdoor federated learning. AISTATS, 2018.
[13] Yang Bai, Xin Yan, Yong Jiang, Shu-Tao Xia, and Yisen Wang. Clustering effect of adversarial robust models. NeurIPS, 2021.
[14] Radu Banabic and George Candea. Fast black-box testing of system recovery code. EuroSys, 2012.
[15] Mohamed Ishmael Belghazi, Aristide Baratin, Sai Rajeshwar, Sherjil Ozair, Yoshua Bengio, Aaron Courville, and Devon Hjelm. Mutual information neural estimation. ICML, 2018.
[16] James Henry Bell, Kallista A Bonawitz, Adrià Gascón, Tancrède Lepoint, and Mariana Raykova. Secure single-server aggregation with (poly) logarithmic overhead. CCS, 2020.
[17] Arjun Nitin Bhagoji, Supriyo Chakraborty, Prateek Mittal, and Seraphin Calo. Analyzing federated learning through an adversarial lens. ICML, 2019.
[18] Keith Bonawitz, Hubert Eichner, Wolfgang Grieskamp, Dzmitry Huba, Alex Ingerman, Vladimir Ivanov, Chloe Kiddon, Jakub Konečnỳ, Stefano Mazzocchi, H Brendan McMahan, et al. Towards federated learning at scale: System design. arXiv preprint, 2019.
[19] Keith Bonawitz, Vladimir Ivanov, Ben Kreuter, Antonio Marcedone, H Brendan McMahan, Sarvar Patel, Daniel Ramage, Aaron Segal, and Karn Seth. Practical secure aggregation for privacy-preserving machine learning. CCS, 2017.
[20] Zhenkun Cai, Xiao Yan, Yidi Wu, Kaihao Ma, James Cheng, and Fan Yu. Dgcl: An efficient communication library for distributed gnn training. EuroSys, 2021.
[21] Zheng Chai, Hannan Fayyaz, Zeshan Fayyaz, Ali Anwar, Yi Zhou, Nathalie Baracaldo, Heiko Ludwig, and Yue Cheng. Towards taming the resource and data heterogeneity in federated learning. {USENIX} OpML, 2019.
[22] Ashutosh Chaubey, Nikhil Agrawal, Kavya Barnwal, Keerat K Guliani, and Pramod Mehta. Universal adversarial perturbations: A survey. arXiv preprint, 2020.
[23] Pin-Yu Chen, Huan Zhang, Yash Sharma, Jinfeng Yi, and Cho-Jui Hsieh. Zoo: Zeroth order optimization based black-box attacks to deep neural networks without training substitute models. ACM AISec, 2017.
[24] Kewei Cheng, Tao Fan, Yilun Jin, Yang Liu, Tianjian Chen, Dimitrios Papadopoulos, and Qiang Yang. Secureboost: A lossless federated learning framework. *IEEE Intelligent Systems*, 2021.
[25] Tat-Seng Chua, Jinhui Tang, Richang Hong, Haojie Li, Zhiping Luo, and Yantao Zheng. NUS-WIDE: a real-world web image database from national university of singapore. In *Proceedings of the ACM international conference on image and video retrieval*, pages 1–9, 2009.
[26] Henggang Cui, Hao Zhang, Gregory R. Ganger, Phillip B. Gibbons, and Eric P. Xing. Geeps: Scalable deep learning on distributed gpus with a gpu-specialized parameter server. EuroSys, 2016.
[27] Anirban Das and Stacy Patterson. Multi-tier federated learning for vertically partitioned data. IEEE ICASSP, 2021.
[28] Arthur P Dempster, Nan M Laird, and Donald B Rubin. Maximum likelihood from incomplete data via the em algorithm. *Journal of the Royal Statistical Society: Series B (Methodological)*, 39(1):1–22, 1977.
[29] Yongheng Deng, Feng Lyu, Ju Ren, Yi-Chao Chen, Peng Yang, Yuezhi Zhou, and Yaoxue Zhang. Fair: Quality-aware federated learning with precise user incentive and model aggregation. INFOCOM, 2021.
[30] Jacob Devlin, Ming-Wei Chang, Kenton Lee, and Kristina Toutanova. BERT: Pre-training of deep bidirectional transformers for language understanding. NAACL, 2019.
[31] Paul Adrien Maurice Dirac. *The principles of quantum mechanics*. Number 27. Oxford university press, 1981.
[32] Minghong Fang, Xiaoyu Cao, Jinyuan Jia, and Neil Gong. Local model poisoning attacks to byzantine-robust federated learning. {USENIX} Security, 2020.
[33] Li Fei-Fei, Rob Fergus, and Pietro Perona. One-shot learning of object categories. IEEE TPAMI, 2006.
[34] Ruth C Fong and Andrea Vedaldi. Interpretable explanations of black boxes by meaningful perturbation. ICCV, 2017.
[35] Chong Fu, Xuhong Zhang, Shouling Ji, Jinyin Chen, Jingzheng Wu, Shanqing Guo, Jun Zhou, Alex X. Liu, and Ting Wang. Label inference attacks against vertical federated learning. {USENIX} Security, 2022.
[36] Clement Fung, Chris JM Yoon, and Ivan Beschastnikh. Mitigating sybils in federated learning poisoning. arXiv preprint, 2018.
[37] Clement Fung, Chris JM Yoon, and Ivan Beschastnikh. The limitations of federated learning in sybil settings. RAID, 2020.
[38] Oded Goldreich. Secure multi-party computation. *Manuscript. Preliminary version*, 78, 1998.
[39] Ian Goodfellow, Yoshua Bengio, Aaron Courville, and Yoshua Bengio. *Deep learning*, volume 1. MIT press Cambridge, 2016.
[40] Ian J Goodfellow, Jonathon Shlens, and Christian Szegedy. Explaining and harnessing adversarial examples. arXiv preprint, 2014.
[41] Yash Goyal, Tejas Khot, Douglas Summers-Stay, Dhruv Batra, and Devi Parikh. Making the v in vqa matter: Elevating the role of image understanding in visual question answering. CVPR, 2017.

[42] Christian Grossmann, Hans-Görg Roos, and Martin Stynes. *Numerical treatment of partial differential equations*, volume 154. Springer, 2007.

[43] Chuan Guo, Jacob Gardner, Yurong You, Andrew Gordon Wilson, and Kilian Weinberger. Simple black-box adversarial attacks. ICML, 2019.

[44] Otkrist Gupta and Ramesh Raskar. Distributed learning of deep neural network over multiple agents. JNCA, 2018.

[45] Andrew Hard, Kanishka Rao, Rajiv Mathews, Swaroop Ramaswamy, Françoise Beaufays, Sean Augenstein, Hubert Eichner, Chloé Kiddon, and Daniel Ramage. Federated learning for mobile keyboard prediction. arXiv preprint, 2018.

[46] Stephen Hardy, Wilko Henecka, Hamish Ivey-Law, Richard Nock, Giorgio Patrini, Guillaume Smith, and Brian Thorne. Private federated learning on vertically partitioned data via entity resolution and additively homomorphic encryption. arXiv preprint, 2017.

[47] Chaoyang He, Songze Li, Jinhyun So, Mi Zhang, Hongyi Wang, Xiaoyang Wang, Praneeth Vepakomma, Abhishek Singh, Hang Qiu, Li Shen, Peilin Zhao, Yan Kang, Yang Liu, Ramesh Raskar, Qiang Yang, Murali Annavaram, and Salman Avestimehr. Fedml: A research library and benchmark for federated machine learning. arXiv preprint, 2020.

[48] Karl Moritz Hermann, Tomáš Kočiskỳ, Edward Grefenstette, Lasse Espeholt, Will Kay, Mustafa Suleyman, and Phil Blunsom. Teaching machines to read and comprehend. arXiv preprint, 2015.

[49] R Devon Hjelm, Alex Fedorov, Samuel Lavoie-Marchildon, Karan Grewal, Phil Bachman, Adam Trischler, and Yoshua Bengio. Learning deep representations by mutual information estimation and maximization. arXiv preprint, 2018.

[50] Andrew Ilyas, Logan Engstrom, Anish Athalye, and Jessy Lin. Black-box adversarial attacks with limited queries and information. ICML, 2018.

[51] Alex Krizhevsky et al. Learning multiple layers of features from tiny images. 2009.

[52] Yann LeCun, Léon Bottou, Yoshua Bengio, and Patrick Haffner. Gradient-based learning applied to document recognition. *Proceedings of the IEEE*, 86(11):2278–2324, 1998.

[53] Jaehoon Lee, Yasaman Bahri, Roman Novak, Samuel S Schoenholz, Jeffrey Pennington, and Jascha Sohl-Dickstein. Deep neural networks as gaussian processes. arXiv preprint, 2017.

[54] Mu Li, David G Andersen, Alexander J Smola, and Kai Yu. Communication efficient distributed machine learning with the parameter server. NeurIPS, 2014.

[55] Tian Li, Maziar Sanjabi, Ahmad Beirami, and Virginia Smith. Fair resource allocation in federated learning. arXiv preprint, 2019.

[56] Xiujun Li, Xi Yin, Chunyuan Li, Pengchuan Zhang, Xiaowei Hu, Lei Zhang, Lijuan Wang, Houdong Hu, Li Dong, Furu Wei, et al. Oscar: Object-semantics aligned pre-training for vision-language tasks. ECCV, 2020.

[57] Tsung-Yi Lin, Michael Maire, Serge Belongie, James Hays, Pietro Perona, Deva Ramanan, Piotr Dollár, and C Lawrence Zitnick. Microsoft COCO: Common objects in context. ECCV, 2014.

[58] Fenglin Liu, Xian Wu, Shen Ge, Wei Fan, and Yuexian Zou. Federated learning for vision-and-language grounding problems. AAAI, 2020.

[59] Yang Liu, Zhihao Yi, and Tianjian Chen. Backdoor attacks and defenses in feature-partitioned collaborative learning. arXiv preprint, 2020.

[60] Jiasen Lu, Jianwei Yang, Dhruv Batra, and Devi Parikh. Hierarchical question-image co-attention for visual question answering. arXiv preprint, 2016.

[61] A Lubna, Saidalavi Kalady, and A Lijiya. MoBVQA: A modality based medical image visual question answering system. IEEE TENCON, 2019.

[62] Jeffrey F Lukman, Huan Ke, Cesar A Stuardo, Riza O Suminto, Daniar H Kurniawan, Dikaimin Simon, Satria Priambada, Chen Tian, Feng Ye, Tanakorn Leesatapornwongsa, et al. Flymc: Highly scalable testing of complex interleavings in distributed systems. EuroSys, 2019.

[63] Xinjian Luo, Yuncheng Wu, Xiaokui Xiao, and Beng Chin Ooi. Feature inference attack on model predictions in vertical federated learning. arXiv preprint, 2020.

[64] Xinjian Luo, Yuncheng Wu, Xiaokui Xiao, and Beng Chin Ooi. Feature inference attack on model predictions in vertical federated learning. ICDE, 2021.

[65] J MacQueen. Classification and analysis of multivariate observations. In *5th Berkeley Symp. Math. Statist. Probability*, pages 281–297, 1967.

[66] Alireza Makhzani, Jonathon Shlens, Navdeep Jaitly, Ian Goodfellow, and Brendan Frey. Adversarial autoencoders. arXiv preprint, 2015.

[67] Ismael Martinez, Sreya Francis, and Abdelhakim Senhaji Hafid. Record and reward federated learning contributions with blockchain. IEEE CyberC, 2019.

[68] Geoffrey J McLachlan and Kaye E Basford. *Mixture models: Inference and applications to clustering*, volume 38. M. Dekker New York, 1988.

[69] Brendan McMahan, Eider Moore, Daniel Ramage, Seth Hampson, and Blaise Aguera y Arcas. Communication-efficient learning of deep networks from decentralized data. AISTATS, 2017.

[70] Seyed-Mohsen Moosavi-Dezfooli, Alhussein Fawzi, Omar Fawzi, and Pascal Frossard. Universal adversarial perturbations. CVPR, 2017.

[71] Nina Narodytska and Shiva Prasad Kasiviswanathan. Simple black-box adversarial perturbations for deep networks. arXiv preprint, 2016.

[72] Milad Nasr, Reza Shokri, and Amir Houmansadr. Comprehensive privacy analysis of deep learning: Passive and active white-box inference attacks against centralized and federated learning. IEEE SP, 2019.

[73] Richard Nock, Stephen Hardy, Wilko Henecka, Hamish Ivey-Law, Giorgio Patrini, Guillaume Smith, and Brian Thorne. Entity resolution and federated learning get a federated resolution. arXiv preprint, 2018.

[74] Shashi Raj Pandey, Nguyen H Tran, Mehdi Bennis, Yan Kyaw Tun, Aunas Manzoor, and Choong Seon Hong. A crowdsourcing framework for on-device federated learning. IEEE TWC, 2020.

[75] Kexin Pei, Yinzhi Cao, Junfeng Yang, and Suman Jana. Deepxplore: Automated whitebox testing of deep learning systems. SOSP, 2017.

[76] Yanghua Peng, Yixin Bao, Yangrui Chen, Chuan Wu, and Chuanxiong Guo. Optimus: An efficient dynamic resource scheduler for deep learning clusters. EuroSys, 2018.

[77] Krishna Pillutla, Sham M Kakade, and Zaid Harchaoui. Robust aggregation for federated learning. arXiv preprint, 2019.

[78] Foster J Provost and Daniel N Hennessy. Scaling up: Distributed machine learning with cooperation. AAAI/IAAI, 1996.

[79] Shaoqing Ren, Kaiming He, Ross Girshick, and Jian Sun. Faster R-CNN: Towards real-time object detection with region proposal networks. IEEE TPAMI, 2016.

[80] Monica Scannapieco, Ilya Figotin, Elisa Bertino, and Ahmed K Elmagarmid. Privacy preserving schema and data matching. SIGMOD, 2007.

[81] Avanti Shrikumar, Peyton Greenside, and Anshul Kundaje. Learning important features through propagating activation differences. ICML, 2017.

[82] Rachael Hwee Ling Sim, Yehong Zhang, Mun Choon Chan, and Bryan Kian Hsiang Low. Collaborative machine learning with incentive-aware model rewards. ICML, 2020.

[83] Karen Simonyan and Andrew Zisserman. Very deep convolutional networks for large-scale image recognition. ICLR, 2015.

[84] Tianshu Song, Yongxin Tong, and Shuyue Wei. Profit allocation for federated learning. IEEE Big Data, 2019.

[85] Ziteng Sun, Peter Kairouz, Ananda Theertha Suresh, and H Brendan McMahan. Can you really backdoor federated learning? arXiv preprint, 2019.

[86] Fnu Suya, Jianfeng Chi, David Evans, and Yuan Tian. Hybrid batch attacks: Finding black-box adversarial examples with limited queries. {USENIX} Security, 2020.

[87] Qi Tian, Kun Kuang, Kelu Jiang, Fei Wu, and Yisen Wang. Analysis and applications of class-wise robustness in adversarial training. KDD, 2021.

[88] Vale Tolpegin, Stacey Truex, Mehmet Emre Gursoy, and Ling Liu. Data poisoning attacks against federated learning systems. ESORICS, 2020.

[89] Kentaroh Toyoda and Allan N Zhang. Mechanism design for an incentive-aware blockchain-enabled federated learning platform. IEEE Big Data, 2019.

[90] Florian Tramèr, Alexey Kurakin, Nicolas Papernot, Ian Goodfellow, Dan Boneh, and Patrick McDaniel. Ensemble adversarial training: Attacks and defenses. arXiv preprint, 2017.

[91] Dimitris Tsipras, Shibani Santurkar, Logan Engstrom, Alexander Turner, and Aleksander Madry. Robustness may be at odds with accuracy. ICLR, 2018.

[92] Hongyi Wang, Kartik Sreenivasan, Shashank Rajput, Harit Vishwakarma, Saurabh Agarwal, Jy-yong Sohn, Kangwook Lee, and Dimitris Papailiopoulos. Attack of the tails: Yes, you really can backdoor federated learning. NeurIPS, 2020.

[93] Lei Wang, Qiang Yin, Chao Tian, Jianbang Yang, Rong Chen, Wenyuan Yu, Zihang Yao, and Jingren Zhou. Flexgraph: A flexible and efficient distributed framework for gnn training. EuroSys, 2021.
[94] Zhibo Wang, Mengkai Song, Zhifei Zhang, Yang Song, Qian Wang, and Hairong Qi. Beyond inferring class representatives: User-level privacy leakage from federated learning. INFOCOM, 2019.
[95] Haiqin Weng, Juntao Zhang, Feng Xue, Tao Wei, Shouling Ji, and Zhiyuan Zong. Privacy leakage of real-world vertical federated learning. arXiv preprint, 2020.
[96] David J Wu, Joe Zimmerman, Jérémy Planul, and John C Mitchell. Privacy-preserving shortest path computation. NDSS, 2016.
[97] Yuncheng Wu, Shaofeng Cai, Xiaokui Xiao, Gang Chen, and Beng Chin Ooi. Privacy preserving vertical federated learning for tree-based models. arXiv preprint, 2020.
[98] Wensheng Xia, Ying Li, Lan Zhang, Zhonghai Wu, and Xiaoyong Yuan. A vertical federated learning framework for horizontally partitioned labels. arXiv preprint, 2021.
[99] Chulin Xie, Keli Huang, Pin-Yu Chen, and Bo Li. Dba: Distributed backdoor attacks against federated learning. ICLR, 2019.
[100] Xiaofei Xie, Lei Ma, Felix Juefei-Xu, Minhui Xue, Hongxu Chen, Yang Liu, Jianjun Zhao, Bo Li, Jianxiong Yin, and Simon See. Deephunter: A coverage-guided fuzz testing framework for deep neural networks. ISSTA, 2019.
[101] Qiang Yang, Yang Liu, Tianjian Chen, and Yongxin Tong. Federated machine learning: Concept and applications. ACM TIST, 2019.
[102] Shuo Yang, Fan Wu, Shaojie Tang, Xiaofeng Gao, Bo Yang, and Guihai Chen. On designing data quality-aware truth estimation and surplus sharing method for mobile crowdsensing. IEEE J-SAC, 2017.
[103] Han Yu, Zelei Liu, Yang Liu, Tianjian Chen, Mingshu Cong, Xi Weng, Dusit Niyato, and Qiang Yang. A fairness-aware incentive scheme for federated learning. AIES, 2020.
[104] Xinhao Yuan and Junfeng Yang. Effective concurrency testing for distributed systems. ASPLOS, 2020.
[105] Michał Zalewski. American Fuzzy Lop. https://lcamtuf.coredump.cx/afl/, 2021.
[106] Rongfei Zeng, Chao Zeng, Xingwei Wang, Bo Li, and Xiaowen Chu. A comprehensive survey of incentive mechanism for federated learning. arXiv preprint, 2021.
[107] Yufeng Zhan, Peng Li, Zhihao Qu, Deze Zeng, and Song Guo. A learning-based incentive mechanism for federated learning. IEEE IoT-J, 2020.
[108] Song Chun Zhu and Alan Yuille. Region competition: Unifying snakes, region growing, and bayes/mdl for multiband image segmentation. IEEE TPAMI, 1996.

APPENDIX A: PROOF OF COROLLARY 1

In this section, we present the detailed proof on the existence of ADIs in HeteroLR and SplitNN.

ADI in HeteroLR. Participant $\mathcal{A}$ holds the data $X_\mathcal{A} \in D_\mathcal{A}$, whereas participant $\mathcal{B}$ holds the data $X_\mathcal{B} \in D_\mathcal{B}$ following any distribution whose density function is $p(X_\mathcal{B})$. $\mathcal{A}$ is controlled by an adversary, whereas $\mathcal{B}$ behaves normally. $\theta_\mathcal{A}$ and $\theta_\mathcal{B}$ are their corresponding coefficients. The HeteroLR f takes $X_\mathcal{A}$ and $X_\mathcal{B}$ as inputs, and its output is:

$$f(X_\mathcal{A}, X_\mathcal{B}) = g(\theta_\mathcal{A}^T X_\mathcal{A} + \theta_\mathcal{B}^T X_\mathcal{B}) \ ,$$

where $X_\mathcal{A} \in \mathbb{R}^{d_1}$, $\theta_\mathcal{A} \in \mathbb{R}^{d_1}$, $X_\mathcal{B} \in \mathbb{R}^{d_2}$, $\theta_\mathcal{B} \in \mathbb{R}^{d_2}$. d_1, d_2 denote dimensions of the features in $\mathcal{A}$ and $\mathcal{B}$, $g(t) = \frac{1}{1+e^{-t}}$ is the Sigmoid function. We have the following corollary:

Corollary 2 (Variance of HeteroLR)**.** *With fixed input $X_\mathcal{A}^*$ and varying input $X_\mathcal{B} \in D_\mathcal{B}$, the output variance of HeteroLR is:*

$$\mathbb{V}_{X_\mathcal{B} \in D_\mathcal{B}}(f(X_\mathcal{A}^*, X_\mathcal{B})) = \sum_{k=1}^{\mathcal{K}} -\frac{\pi_k}{\sqrt{2\pi}} \frac{1}{\sqrt{\sigma_k'^2 + \sigma_2^2}} \exp\{-\frac{1}{2}\frac{\mu_k'^2}{\sigma_k'^2 + \sigma_2^2}\}$$
$$+ \sum_{k=1}^{\mathcal{K}} \pi_k \, \Phi(\frac{\mu_k'}{\sqrt{\sigma_1^2 + \sigma_k'^2}})(1 - \sum_{k=1}^{\mathcal{K}} \pi_k \, \Phi(\frac{\mu_k'}{\sqrt{\sigma_1^2 + \sigma_k'^2}})) \ ,$$

where the density function $p(X_\mathcal{B})$ is approximated by Gaussian Mixture Model: $p(X_\mathcal{B}) \approx \sum_{k=1}^{\mathcal{K}} \pi_k \mathcal{N}(X_\mathcal{B}|\boldsymbol{\mu_k}, \boldsymbol{\Sigma_k})$, $\sum_{k=1}^{\mathcal{K}} \pi_k = 1$, $\pi_k > 0$, $\mathcal{K}$ is a finite number, $\boldsymbol{\mu_k} \in \mathbb{R}^{d_2}$, $\boldsymbol{\Sigma_k} \in \mathbb{R}^{d_2 \times d_2}$, $\mu_k' = \theta_\mathcal{A}^T X_\mathcal{A}^* + \theta_\mathcal{B}^T \boldsymbol{\mu_k}$, $\sigma_k'^2 = \theta_\mathcal{B}^T \boldsymbol{\Sigma_k} \theta_\mathcal{B}$, Φ is the cumulative distribution function (CDF) of the standard normal distribution, $\sigma_1 = 1.699$, and $\sigma_2 = 1.630$.

Proof. Let $S = \theta_\mathcal{A}^T X_\mathcal{A}^* + \theta_\mathcal{B}^T X_\mathcal{B}$. Thus, $f(X_\mathcal{A}^*, X_\mathcal{B}) = g(S)$. Aligned with the conventions [15, 33, 49, 53, 66, 108] in machine learning, we use Gaussian mixture model [68] and Expectation Maximization [28] to approximate the density function $p(X_\mathcal{B})$. Note that GMMs can approximate any smooth distributions [39].

$$p(X_\mathcal{B}) \approx \sum_{k=1}^{\mathcal{K}} \pi_k \mathcal{N}(X_\mathcal{B}|\boldsymbol{\mu_k}, \boldsymbol{\Sigma_k}) \ ,$$

where $\sum_{k=1}^{\mathcal{K}} \pi_k = 1$, $\pi_k > 0$, $\mathcal{K}$ is a finite number, $\boldsymbol{\mu_k} \in \mathbb{R}^{d_2}$ and $\boldsymbol{\Sigma_k} \in \mathbb{R}^{d_2 \times d_2}$. If $p(X_\mathcal{B})$ is discrete and not smooth (e.g. $X_\mathcal{B}$ is categorical data), we can approximate it by taking $\boldsymbol{\Sigma_k} \to \mathbf{0}$ and $\mathcal{K}$ becomes the total number of distinct data in $X_\mathcal{B}$, the Gaussian distribution density would become a Dirac delta function [31] and the following calculations still hold.

Further, we can obtain the density function of S as: $p(S) = \sum_{k=1}^{\mathcal{K}} \pi_k \mathcal{N}(S|\theta_\mathcal{A}^T X_\mathcal{A}^* + \theta_\mathcal{B}^T \boldsymbol{\mu_k}, \theta_\mathcal{B}^T \boldsymbol{\Sigma_k} \theta_\mathcal{B})$. Taking $\mu_k' = \theta_\mathcal{A}^T X_\mathcal{A}^* + \theta_\mathcal{B}^T \boldsymbol{\mu_k}$ and $\sigma_k'^2 = \theta_\mathcal{B}^T \boldsymbol{\Sigma_k} \theta_\mathcal{B}$, we thus calculate the expected value of the output:

$$\mathbb{E}_{X_\mathcal{B} \in D_\mathcal{B}}(g(S)) = \int g(t) \sum_{k=1}^{\mathcal{K}} \pi_k \mathcal{N}(t|\mu_k', \sigma_k'^2) \, dt$$
$$\approx \int \sum_{k=1}^{\mathcal{K}} \pi_k \, \Phi(\frac{t}{\sigma_1}) \mathcal{N}(t|\mu_k', \sigma_k'^2) \, dt = \sum_{k=1}^{\mathcal{K}} \pi_k \, \Phi(\frac{\mu_k'}{\sqrt{\sigma_1^2 + \sigma_k'^2}}) \quad (5)$$

Here, the $g(t)$ is approximated by the cumulative distribution function of standard Gaussian distribution and parameter σ_1

as $\Phi(\frac{t}{\sigma_1})$, where $\sigma_1 = 1.699$ to minimize the L^2 error. The variance of the output is calculated as follows:

$$\begin{aligned}\mathbb{V}_{X_{\mathcal{B}}\in D_{\mathcal{B}}}(g(S)) &= \langle g(S)^2\rangle - \langle g(S)\rangle^2 \\ &= \langle g(S) - g(S)(1-g(S))\rangle - \langle g(S)\rangle^2 \\ &= \langle g(S)\rangle\left(1-\langle g(S)\rangle\right) - \langle g'(S)\rangle\ ,\end{aligned} \tag{6}$$

where $\langle\cdot\rangle$ donates $\mathbb{E}_{X_{\mathcal{B}}\in D_{\mathcal{B}}}(\cdot)$. Further, we approximate the derivation of Sigmoid function $g'(S)$ using the pdf of Gaussian distribution. When the L^2 error is minimized, we get the approximated function of $g'(S)$ with $\sigma_2 = 1.630$:

$$g'(S) \approx \frac{1}{\sqrt{2\pi}\sigma_2}\exp\{-\frac{S^2}{2\sigma_2^2}\}$$

Further, we can calculate the expected value of the derivation of Sigmoid function:

$$\begin{aligned}\mathbb{E}_{X_{\mathcal{B}}\in D_{\mathcal{B}}}(g'(S)) &= \int\sum_{k=1}^{\mathcal{K}}\frac{\pi_k}{2\pi\sigma'_k\sigma_2}\exp\{-\frac{t^2}{2\sigma_2^2}-\frac{(t-\mu'_k)^2}{2\sigma'^2_k}\}dt \\ &= \sum_{k=1}^{\mathcal{K}}\frac{\pi_k}{\sqrt{2\pi}}\frac{1}{\sqrt{\sigma'^2_k+\sigma_2^2}}\exp\{-\frac{1}{2}\frac{\mu'^2_k}{\sigma'^2_k+\sigma_2^2}\}\end{aligned} \tag{7}$$

According to Eq. 5, 6 and 7:

$$\begin{aligned}\mathbb{V}_{X_{\mathcal{B}}\in D_{\mathcal{B}}}(g(S)) = &\sum_{k=1}^{\mathcal{K}} -\frac{\pi_k}{\sqrt{2\pi}}\frac{1}{\sqrt{\sigma'^2_k+\sigma_2^2}}\exp\{-\frac{1}{2}\frac{\mu'^2_k}{\sigma'^2_k+\sigma_2^2}\} \\ &+\sum_{k=1}^{\mathcal{K}}\pi_k\,\Phi(\frac{\mu'_k}{\sqrt{\sigma_1^2+\sigma'^2_k}})(1-\sum_{k=1}^{\mathcal{K}}\pi_k\,\Phi(\frac{\mu'_k}{\sqrt{\sigma_1^2+\sigma'^2_k}}))\end{aligned}$$

□

With unbounded $X^*_{\mathcal{A}}$ and $||\theta_{\mathcal{A}}||_1 > 0$, the range of $\theta^T_{\mathcal{A}}X^*_{\mathcal{A}}$ is $(-\infty,+\infty)$. Thus, $\lim_{\theta^T_{\mathcal{A}}X^*_{\mathcal{A}}\to-\infty}\mu'_k = -\infty$ and $\lim_{\mu'_k\to-\infty}\mathbb{V}_{X_{\mathcal{B}}\in D_{\mathcal{B}}}(f(X^*_{\mathcal{A}},X_{\mathcal{B}})) = 0^+$. For any $\epsilon > 0$, there exists $X^*_{\mathcal{A}}$ satisfying $\mathbb{V}_{X_{\mathcal{B}}\in D_{\mathcal{B}}}(f(X^*_{\mathcal{A}},X_{\mathcal{B}})) \le \epsilon$. According to Def. 1, $X^*_{\mathcal{A}}$ is an ADI for HeteroLR.

ADI in SplitNN. Similarly, in SplitNN, $X_{\mathcal{A}} \in D_{\mathcal{A}}$ and $X_{\mathcal{B}} \in D_{\mathcal{B}}$ are the corresponding local outputs from participants $\mathcal{A}$ and $\mathcal{B}$, and the coordinator model is a single-layer fully connected network, with ReLU as its activation function. SplitNN f takes $X_{\mathcal{A}}$ and $X_{\mathcal{B}}$ as inputs, and its output is:

$$f(X_{\mathcal{A}},X_{\mathcal{B}}) = ReLU(w^T\,[X_{\mathcal{A}}\,||\,X_{\mathcal{B}}]) = ReLU(w^T_{\mathcal{A}}X_{\mathcal{A}} + w^T_{\mathcal{B}}X_{\mathcal{B}}),$$

where $||$ is concatenation and w denotes the parameter of the coordinator model. $X_{\mathcal{A}} \in \mathbb{R}^{d_1}$, $w_{\mathcal{A}} \in \mathbb{R}^{d_1}$, $X_{\mathcal{B}} \in \mathbb{R}^{d_2}$ and $w_{\mathcal{B}} \in \mathbb{R}^{d_2}$. d_1, d_2 are dimensions of the outputs in $\mathcal{A}$ and $\mathcal{B}$. $X_{\mathcal{B}}$ follows any distribution whose density function is $p(X_{\mathcal{B}})$. We have the following corollary.

Corollary 3 (Variance of SplitNN)**.** *With fixed input $X^*_{\mathcal{A}}$ and varying input $X_{\mathcal{B}} \in D_{\mathcal{B}}$, the output variance of SplitNN is:*

$$\begin{aligned}&\mathbb{V}_{X_{\mathcal{B}}\in D_{\mathcal{B}}}(f(X^*_{\mathcal{A}},X_{\mathcal{B}})) \\ &= (\sum_{k=1}^{\mathcal{K}}\pi_k\,\Phi(\frac{\mu'_k}{\sigma'_k}))(\sum_{k=1}^{\mathcal{K}}\pi_k^2\,\sigma'^2_k(1-\frac{\mu'_k}{\sigma'_k}\frac{\phi(\frac{\mu'_k}{\sigma'_k})}{\Phi(\frac{\mu'_k}{\sigma'_k})}-(\frac{\phi(\frac{\mu'_k}{\sigma'_k})}{\Phi(\frac{\mu'_k}{\sigma'_k})})^2) \\ &+(\sum_{k=1}^{\mathcal{K}}\pi_k\,(\mu'_k+\sigma'_k\frac{\phi(\frac{\mu'_k}{\sigma'_k})}{\Phi(\frac{\mu'_k}{\sigma'_k})}))^2(1-\sum_{k=1}^{\mathcal{K}}\pi_k\,\Phi(\frac{\mu'_k}{\sigma'_k}))),\end{aligned}$$

where $p(X_{\mathcal{B}})$ is approximated by Gaussian Mixture Model: $p(X_{\mathcal{B}}) \approx \sum_{k=1}^{\mathcal{K}}\pi_k\,\mathcal{N}(X_{\mathcal{B}}|\boldsymbol{\mu_k},\boldsymbol{\Sigma_k})$, $\sum_{k=1}^{\mathcal{K}}\pi_k = 1$, $\pi_k > 0$, $\mathcal{K}$ is a finite number, $\mu'_k = w^T_{\mathcal{A}}X^*_{\mathcal{A}} + w^T_{\mathcal{B}}\boldsymbol{\mu_k}$, $\sigma'^2_k = w^T_{\mathcal{B}}\boldsymbol{\Sigma_k}\,w_{\mathcal{B}}$, and Φ is the CDF of the standard normal distribution.

Proof. Similar to the proof of Cor. 2, for any distribution of $X_{\mathcal{B}}$, we use Gaussian mixture model and Expectation Maximization to approximate its density function $p(X_{\mathcal{B}})$ as:

$$p(X_{\mathcal{B}}) \approx \sum_{k=1}^{\mathcal{K}}\pi_k\,\mathcal{N}(X_{\mathcal{B}}|\boldsymbol{\mu_k},\boldsymbol{\Sigma_k})\ ,$$

where $\sum_{k=1}^{\mathcal{K}}\pi_k = 1$, $\pi_k > 0$, $\mathcal{K}$ is a finite number, $\boldsymbol{\mu_k} \in \mathbb{R}^{d_2}$ and $\boldsymbol{\Sigma_k} \in \mathbb{R}^{d_2\times d_2}$. Similarly, if $p(X_{\mathcal{B}})$ is highly discrete, we can approximate it by taking $\boldsymbol{\Sigma_k} \to \mathbf{0}$.

For fixed $X^*_{\mathcal{A}}$, let $Y = w^T_{\mathcal{A}}X^*_{\mathcal{A}} + w^T_{\mathcal{B}}X_{\mathcal{B}}$, $\mu'_k = w^T_{\mathcal{A}}X^*_{\mathcal{A}} + w^T_{\mathcal{B}}\boldsymbol{\mu_k}$, and $\sigma'^2_k = w^T_{\mathcal{B}}\boldsymbol{\Sigma_k}\,w_{\mathcal{B}}$. Then, $p(Y) = \sum_{k=1}^{\mathcal{K}}\pi_k\,\mathcal{N}(Y|\mu'_k,\sigma'^2_k)$. We have:

$$\mathbb{E}_{X_{\mathcal{B}}\in D_{\mathcal{B}}}(Y|Y>0) = \sum_{k=1}^{\mathcal{K}}\pi_k\,(\mu'_k+\sigma'_k\frac{\phi(\frac{\mu'_k}{\sigma'_k})}{\Phi(\frac{\mu'_k}{\sigma'_k})}) \tag{8}$$

$$\mathcal{P}(Y>0) = \sum_{k=1}^{\mathcal{K}}\pi_k\,\Phi(\frac{\mu'_k}{\sigma'_k}) \tag{9}$$

And we get the expected central coordinator output:

$$\begin{aligned}\mathbb{E}_{X_{\mathcal{B}}\in D_{\mathcal{B}}}(f(X^*_{\mathcal{A}},X_{\mathcal{B}})) &= \mathbb{E}_{X_{\mathcal{B}}\in D_{\mathcal{B}}}(Y|Y>0)\times\mathcal{P}(Y>0) \\ &= (\sum_{k=1}^{\mathcal{K}}\pi_k\,(\mu'_k+\sigma'_k\frac{\phi(\frac{\mu'_k}{\sigma'_k})}{\Phi(\frac{\mu'_k}{\sigma'_k})}))\,(\sum_{k=1}^{\mathcal{K}}\pi_k\,\Phi(\frac{\mu'_k}{\sigma'_k}))\end{aligned} \tag{10}$$

The variance of the truncated mixture Gaussian distribution:

$$\mathbb{V}_{X_{\mathcal{B}}\in D_{\mathcal{B}}}(Y|Y>0) = \sum_{k=1}^{\mathcal{K}}\pi_k^2\,\sigma'^2_k(1-\frac{\mu'_k}{\sigma'_k}\frac{\phi(\frac{\mu'_k}{\sigma'_k})}{\Phi(\frac{\mu'_k}{\sigma'_k})}-(\frac{\phi(\frac{\mu'_k}{\sigma'_k})}{\Phi(\frac{\mu'_k}{\sigma'_k})})^2) \tag{11}$$

According to Eq. 8, 9, 10 and 11, we have:

$$\mathbb{E}_{X_{\mathcal{B}}\in D_{\mathcal{B}}}(Y^2|Y>0) = \mathbb{V}_{X_{\mathcal{B}}\in D_{\mathcal{B}}}(Y|Y>0) + (\mathbb{E}_{X_{\mathcal{B}}\in D_{\mathcal{B}}}(Y|Y>0))^2$$

Therefore, the variance of the coordinator model's output is:

$$\begin{aligned}\mathbb{V}_{X_{\mathcal{B}}\in D_{\mathcal{B}}}(f(X^*_{\mathcal{A}},X_{\mathcal{B}})) &= \mathbb{E}_{X_{\mathcal{B}}\in D_{\mathcal{B}}}(Y^2|Y>0)\times\mathcal{P}(Y>0) \\ &\quad-(\mathbb{E}_{X_{\mathcal{B}}\in D_{\mathcal{B}}}(f(X^*_{\mathcal{A}},X_{\mathcal{B}})))^2 \\ &=(\sum_{k=1}^{\mathcal{K}}\pi_k\,\Phi(\frac{\mu'_k}{\sigma'_k}))\,(\sum_{k=1}^{\mathcal{K}}\pi_k^2\,\sigma'^2_k(1-\frac{\mu'_k}{\sigma'_k}\frac{\phi(\frac{\mu'_k}{\sigma'_k})}{\Phi(\frac{\mu'_k}{\sigma'_k})}-(\frac{\phi(\frac{\mu'_k}{\sigma'_k})}{\Phi(\frac{\mu'_k}{\sigma'_k})})^2) \\ &\quad+(\sum_{k=1}^{\mathcal{K}}\pi_k\,(\mu'_k+\sigma'_k\frac{\phi(\frac{\mu'_k}{\sigma'_k})}{\Phi(\frac{\mu'_k}{\sigma'_k})}))^2(1-\sum_{k=1}^{\mathcal{K}}\pi_k\,\Phi(\frac{\mu'_k}{\sigma'_k})))\end{aligned}$$

□

According to Cor. 3, with unbounded $X^*_{\mathcal{A}}$ and $||w_{\mathcal{A}}||_1 > 0$, the range of $w^T_{\mathcal{A}}X^*_{\mathcal{A}}$ is $(-\infty,+\infty)$. Thus, $\lim_{w^T_{\mathcal{A}}X^*_{\mathcal{A}}\to-\infty}\mu'_k = -\infty$ and $\lim_{\mu'_k\to-\infty}\mathbb{V}_{X_{\mathcal{B}}\in D_{\mathcal{B}}}(f(X^*_{\mathcal{A}},X_{\mathcal{B}})) = 0^+$. For any $\epsilon > 0$, there must exists $X^*_{\mathcal{A}}$ satisfying $\mathbb{V}_{X_{\mathcal{B}}\in D_{\mathcal{B}}}(f(X^*_{\mathcal{A}},X_{\mathcal{B}})) \le \epsilon$. Thus, according to Def. 1, $X^*_{\mathcal{A}}$ is an ADI for SplitNN.

Appendix B: Proof on the Existence of ADIs Using Bounded Mutation

In line with the proof given in Sec. III by arbitrarily mutating inputs, this section presents the following proof on the existence of ADIs using bounded mutation.

Proof. Let $X^*_{\mathcal{A}}$ be bounded by a space $\mathcal{S}_{\mathcal{A}}$ in $d_{\mathcal{A}}$ dimension, $X^*_{\mathcal{A}} \in \mathcal{S}_{\mathcal{A}}$. For HeteroLR, μ'_ks are linear combinations of

features in $X^*_{\mathcal{A}}$; therefore, they are also bounded by two limited real numbers: $\mu'_k \in [\mu'_{min}, \mu'_{max}]$. Further, the ratio $\frac{\mu'_k}{\sqrt{\sigma_1^2+\sigma_k'^2}}$ is bounded by $[r_{min}, r_{max}]$ and the variance is also bounded:

$$\begin{aligned}\mathbb{V}_{X_{\mathcal{B}}\in D_{\mathcal{B}}}(g(S)) &= \sum_{k=1}^{\mathcal{K}} -\frac{\pi_k}{\sqrt{2\pi}}\frac{1}{\sqrt{\sigma_k'^2+\sigma_2^2}}\exp\{-\frac{1}{2}\frac{\mu_k'^2}{\sigma_k'^2+\sigma_2^2}\} \\ &+ \sum_{k=1}^{\mathcal{K}}\pi_k\,\Phi(\frac{\mu'_k}{\sqrt{\sigma_1^2+\sigma_k'^2}})(1-\sum_{k=1}^{\mathcal{K}}\pi_k\,\Phi(\frac{\mu'_k}{\sqrt{\sigma_1^2+\sigma_k'^2}})) \\ &< \sum_{k=1}^{\mathcal{K}}\pi_k\,\Phi(\frac{\mu'_k}{\sqrt{\sigma_1^2+\sigma_k'^2}}) - \frac{1}{\mathcal{K}}(\sum_{k=1}^{\mathcal{K}}\pi_k\,\Phi(\frac{\mu'_k}{\sqrt{\sigma_1^2+\sigma_k'^2}}))^2 \\ &< \Phi(r_{max}) - \frac{1}{\mathcal{K}}\Phi(r_{max})^2\end{aligned}$$

If r_{max} satisfies $\Phi(r_{max}) \leq \frac{\mathcal{K}+\sqrt{\mathcal{K}^2-4\epsilon\mathcal{K}}}{2}$, the variance must be bounded by ϵ, $\mathbb{V}_{X_{\mathcal{B}}\in D_{\mathcal{B}}}(g(S)) \leq \epsilon$, which means the ADI $X^*_{\mathcal{A}}$ generated by bounded mutation exists.

Similarly, for SplitNN, μ'_ks are also bounded, $\mu'_k \in [\mu'_{min}, \mu'_{max}]$. Similarly, $\sigma'_k \in [\sigma'_{min}, \sigma'_{max}]$ and $\frac{\mu_k}{\sigma'_k} \in [r_{min}, r_{max}]$. When $\mu'_k \leq 0$, the variance is bounded by:

$$\begin{aligned}\mathbb{V}_{X_{\mathcal{B}}\in D_{\mathcal{B}}}(f(X^*_{\mathcal{A}}, X_{\mathcal{B}})) &= \mathbb{E}_{X_{\mathcal{B}}\in D_{\mathcal{B}}}(Y^2|Y>0)\times\mathcal{P}(Y>0) \\ &\quad - (\mathbb{E}_{X_{\mathcal{B}}\in D_{\mathcal{B}}}(f(X^*_{\mathcal{A}}, X_{\mathcal{B}})))^2 \\ &= (\mathbb{E}_{X_{\mathcal{B}}\in D_{\mathcal{B}}}(Y|Y>0))^2\times\mathcal{P}(Y>0)(1-\mathcal{P}(Y>0)) \\ &\quad + \mathbb{V}_{X_{\mathcal{B}}\in D_{\mathcal{B}}}(Y|Y>0)\times\mathcal{P}(Y>0) \\ &\leq \mathbb{V}_{X_{\mathcal{B}}\in D_{\mathcal{B}}}(Y|Y>0)\times\Phi(r_{max}) + \frac{1}{4}(\mathbb{E}_{X_{\mathcal{B}}\in D_{\mathcal{B}}}(Y|Y>0))^2 \\ &< \Phi(r_{max}) + \frac{1}{4}\Phi(r_{max})\mu_{min}'^2 + \frac{1}{4}\mu_{max}'^2 + \frac{1}{4}\sigma_{max}'^2\frac{\phi(r_{max})^2}{\Phi(r_{min})^2}\end{aligned}$$

If the boundaries satisfy:

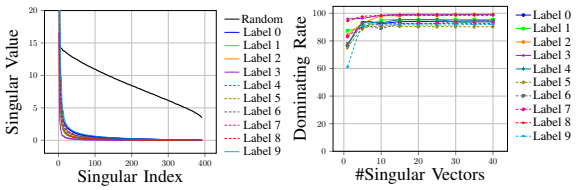
$$\Phi(r_{max}) + \frac{1}{4}\Phi(r_{max})\mu_{min}'^2 + \frac{1}{4}\mu_{max}'^2 + \frac{1}{4}\sigma_{max}'^2\frac{\phi(r_{max})^2}{\Phi(r_{min})^2} \leq \epsilon\,,$$

the variance must be bounded by ϵ: $\mathbb{V}_{X_{\mathcal{B}}\in D_{\mathcal{B}}}(f(x^*_{\mathcal{A}}, x_{\mathcal{B}})) \leq \epsilon$. Thus, the ADI $X^*_{\mathcal{A}}$ generated by bounded mutation exists. □

Appendix C: Further Discussion

Attack on Tree-based Models. This paper examines parameterized VFL systems. In tree-based VFL systems [24, 97], each of the parties will hold several nodes of the tree. The structure of the malicious participant's tree is explicitly revealed, allowing them to easily modify their inputs to reach the target node of their tree and control the output at their will. However, if some inputs from the other participants never reach the malicious participant's node, they cannot dominate the outputs of those inputs. We deem it an interesting future work to study ADIs in tree-based VFL.

Selection of $\mathcal{S}$. In evaluation, we select $\mathcal{S}$ from the test dataset of $\mathcal{B}$ randomly. According to our analysis in Sec. IV-A and our evaluation, we don't have strict requirements for $\mathcal{S}$; randomly selecting $\mathcal{S}$ is sufficient to synthesize ADIs. However, if $\mathcal{S}$ is highly biased (e.g., the labels of samples in $\mathcal{S}$ are the same), then the success rate would be lower. In practice, attackers can manually check the distribution of $\mathcal{S}$ to avoid a highly biased situation. We deem it an interesting topic to further study generating ADIs using biased $\mathcal{S}$.



(a) Singular values. (b) Reconstructed results.

Fig. 9: Singular values and reconstructed results using different numbers of singular vectors on MNIST.

Limitations. In Sec. VII-E, we show that the attacker can successfully synthesize ADIs in the setting where the attacker only knows the input range of the benign participants. However, if the attacker has no information on the benign participants' data, ADIs cannot be successfully synthesized.

Also, in our threat model (Sec. III-B), the attacker can comprise a small group of users, and upload their data to $\mathcal{B}$ for further inference (not for training). Note that to accomplish this step, users can either replace their existing data with $X^i_{\mathcal{B}} + \delta$, or create a new account with $X^i_{\mathcal{B}} + \delta$, where δ is the small perturbation introduced in Sec. IV-B. Given that said, we agree this may be uncovered if the participants in VFL spend large efforts investigating the users' input data when conducting model inference (though the strategy is unclear to us at this moment). We deem this feasibility as a potential mitigation of our attack.

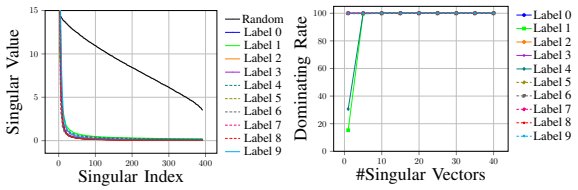
Appendix D: Exploring The Size of $\mathcal{S}$

Synthesizing ADIs requires preparing a sample dataset $\mathcal{S}$ that follows the distribution of $\mathcal{B}$'s standard inputs. $|\mathcal{S}|$ is 20 for the above experiments, meaning that we *randomly* select 20 sample inputs from the test dataset of $\mathcal{B}$ to form $\mathcal{S}$. This section explores how $|\mathcal{S}|$ influences ADI synthesis.

We use MNIST and CIFAR-10 over two participants $\mathcal{A}$ and $\mathcal{B}$. In particular, we randomly select ten $X^*_{\mathcal{A}}$ as the inputs of $\mathcal{A}$. These ten $X^*_{\mathcal{A}}$ will be classified into labels 0–9 and we confirm that they behave normally and do not dominate the joint inference. We further launch ADI synthesis with bounded mutation to generate an ADI from each $X^*_{\mathcal{A}}$. Model configuration and the feature partition ratio over $\mathcal{A}$ and $\mathcal{B}$ are aligned with evaluation in Sec. VII-A, and the dominating threshold is set as 95%.

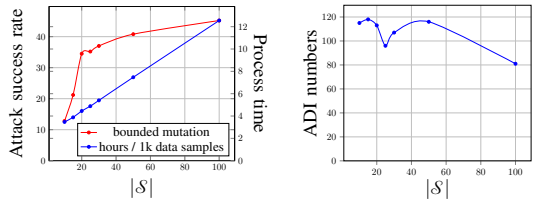
Recall to synthesize an ADI from $X^*_{\mathcal{A}}$, we iterate each data $X^i_{\mathcal{B}}$ in $\mathcal{S}$ and compute a perturbation vector V_i (see Alg. 1). Each V_i points toward the direction of the adversary-specified classification region $R_{l_{target}}$. Let h be the size of $\mathcal{S}$, to quantify the correlation between h perturbation vectors, we first define the matrix: $N = \left[\frac{V_1}{||V_1||_2} \cdots \frac{V_h}{||V_h||_2}\right]$.

To analyze the correlation of perturbation vectors, we use entire test datasets to form matrix N. Fig. 9a and Fig. 10a report the singular values. Compared with the matrix uniformly sampled at random from the unit sphere, singular values of N decay faster. This indicates the existence of primary correlations and redundancies in mutations launched during ADI synthesis using different inputs of $\mathcal{B}$. This also implies there



(a) Singular values. (b) Reconstructed results.

Fig. 10: Singular values and reconstructed results using different numbers of singular vectors on CIFAR-10.



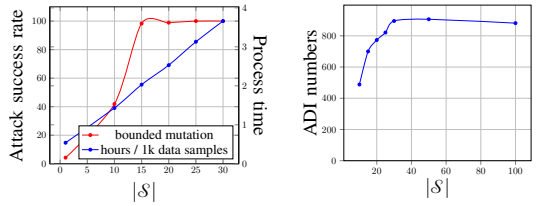
(a) ADI synthesis. (b) Fuzz testing.

Fig. 11: Performance under different $|\mathcal{S}|$ on MNIST.

exists a low dimensional subspace that sufficiently captures the correlations among different inputs of $\mathcal{B}$.

We thus hypothesize that ADI exists because of a low-dimensional subspace that captures correlations between different classification regions. To test our hypothesis, we reconstruct the mutation using different numbers of singular vectors in decreasing order of their singular values and test the ADI dominating rates by perturbing $X^*_{\mathcal{A}}$. Fig. 9b and Fig. 10b report the results: mutations reconstructed using only five singular vectors already reach high dominating rates (over 80% for MNIST and close to 100% for CIFAR-10), and ten singular vectors with the highest singular values obtain close to 90% dominating rates for MNIST and close to 100% for CIFAR-10. The results are consistent on the datasets we evaluate. We interpret that the results support our hypothesis. This hypothesis also explains that most perturbations are heading to a similar direction. Therefore, we do not need a large $|\mathcal{S}|$ to successfully generate ADIs.

We further evaluate how $|\mathcal{S}|$ influences ADI generation, whose results are in Fig. 11 and Fig. 12. The ADI synthesis follows Sec. VII-A. Fuzzing is launched for 12 hours for different $|\mathcal{S}|$ and we record the number of discovered ADIs. As expected, Fig. 11a and Fig. 12a show that larger $|\mathcal{S}|$ leads to increased success rates in synthesizing ADIs. However, as seen in the blue lines of Fig. 11a and Fig. 12a, ADI synthesis takes substantially longer time as $|\mathcal{S}|$ increases (we report the total time taken by perturbing 1,000 inputs of $\mathcal{A}$). Recall



(a) ADI synthesis. (b) Fuzz testing.

Fig. 12: Performance under different $|\mathcal{S}|$ on CIFAR-10.

given a normal input of $\mathcal{A}$, we iterate every element in $\mathcal{S}$ to compute the perturbation vector, which explains the linear growth of processing time in Fig. 11a and Fig. 12a. We have similar observations in Fig. 11b and Fig. 12b. Overall, while larger $|\mathcal{S}|$ may increase the likelihood of generating ADIs (as in Fig. 11a and Fig. 12a), it may also limit the fuzzing throughput. It is seen that the "sweet spot" is around 15–20 in Fig. 11b for the medium complex MNIST dataset. For the complex dataset CIFAR-10, we find that $|\mathcal{S}|$ between 20 and 50 are good for our setting. The range is a bit larger than that of MNIST, given that CIFAR-10 has a larger feature space. Overall, fuzzing can be boosted by taking a slightly larger $|\mathcal{S}|$, such that the mutation vector can capture contributions of $\mathcal{B}$ for different input data more accurately. Consistent with MNIST, the number of found ADIs for CIFAR-10 is starting to decrease when $|\mathcal{S}|$ is greater than 50, since an overly large $|\mathcal{S}|$ limits the fuzzing throughput.

Determining $|\mathcal{S}|$ should take the VFL task specification, feature dimensions, and protocol complexity into account. Moreover, we emphasize that synthesizing ADIs does not require a large $|\mathcal{S}|$: as in Fig. 9a and Fig. 10a, perturbations applied toward different data samples are highly correlated.

Appendix E: Rewards Estimation

Several schemes are proposed to analyze the fairness and rewarding in federated learning and collaborative machine learning [81, 82, 84, 102, 103]. Despite the difference in implementations, they primarily assess the importance of a participant's contribution in a joint prediction. The VFL frameworks we evaluated do not offer an "out-of-the-box" rewarding estimation module. Therefore, to estimate rewards for each participant in a joint inference, we take a general approach to measuring the L_1 norm of the saliency map (line 3 in Alg. 1) derived from each participant's input data.

Table XI reports the normalized estimated rewards for different datasets. To generate ADIs, we use bounded mutation at the 95% threshold. It's easy to see that given normal inputs used by both ends, each participant is estimated to receive approximately the same reward (except VFVQA; see discussion below). For instance, given one unit of reward offered for each joint inference over NUS-WIDE, $\mathcal{A}$ and $\mathcal{B}$ anticipate receiving 0.492 and 0.508 units of rewards, respectively. In contrast, when $\mathcal{A}$ uses ADIs, $\mathcal{A}$ can receive 0.859 units of rewards for at least 95% of joint inferences. This is consistent with our discussion in Sec. III-B.

For VQA v2.0, we observe that the contribution of $\mathcal{B}$ drops when $\mathcal{A}$ uses ADIs. However, we clarify that results in Table XI indeed *underestimate* the dominance of ADIs. Recall for this VFVQA task, $\mathcal{B}$ raises natural-language questions toward images possessed by $\mathcal{A}$. The gradients of natural-language question inputs in VFVQA measure the *local* sensitivity of the VFVQA system. However, different from other tasks, the perturbed questions will not form reasonable text if they are only perturbed by gradients measuring local sensitivity. This explains why the contribution of $\mathcal{B}$ in Table XI, even for normal inputs, is larger than $\mathcal{A}$.

TABLE XI: Contribution Estimation.

		$\mathcal{A}$	$\mathcal{B}$
NUS-WIDE	Normal Inputs Used by Both Sides	0.492	0.508
	ADIs in $\mathcal{A}$, Normal Inputs in $\mathcal{B}$	0.859	0.141
Credit	Normal Inputs Used by Both Sides	0.457	0.543
	ADIs in $\mathcal{A}$, Normal Inputs in $\mathcal{B}$	0.856	0.144
Vehicle	Normal Inputs Used by Both Sides	0.504	0.496
	ADIs in $\mathcal{A}$, Normal Inputs in $\mathcal{B}$	0.784	0.216
MNIST	Normal Inputs Used by Both Sides	0.429	0.571
	ADIs in $\mathcal{A}$, Normal Inputs in $\mathcal{B}$	0.833	0.167
VQA v2.0	Normal Inputs Used by Both Sides	0.279	0.721
	ADIs in $\mathcal{A}$, Normal Inputs in $\mathcal{B}$	0.352	0.648
CIFAR-10	Normal Inputs Used by Both Sides	0.425	0.575
	ADIs in $\mathcal{A}$, Normal Inputs in $\mathcal{B}$	0.748	0.252

TABLE XII: Dominating rates of the standard dataset under different feature partition ratios.

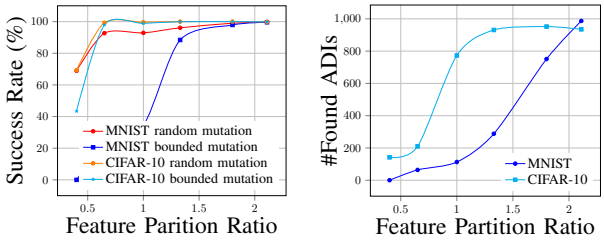
Dataset	Feature Partition Ratio	Dominating Rate on $\mathcal{A}$	Dominating Rate on $\mathcal{B}$	Model Accuracy on Test Datasets
MNIST	**0.40**	0.00%	94.30%	97.55%
	0.65	0.00%	20.49%	97.81%
	1.00	0.87%	0.43%	97.78%
	1.33	5.79%	0.00%	98.01%
	1.80	50.40%	0.00%	98.20%
	2.11	72.40%	0.00%	97.62%
CIFAR-10	**0.40**	0.00%	47.6%	86.56%
	0.65	0.30%	31.0%	86.34%
	1.00	2.63%	7.20%	86.55%
	1.33	13.9%	2.10%	86.22%
	1.80	31.3%	0.10%	86.21%
	2.11	36.2%	0.10%	86.38%

While studies on assessing attention to natural-language questions or images exist [48, 60], comparing their contribution is an open problem. We follow [41] to approximate and compare their contributions. The approach proposed by [41] is conceptually consistent with our evaluation in Sec. VII, where the questions or images are replaced by other data samples in the dataset to see how these replacements will influence the joint inference. We report that when using this method to compare the contributions of $\mathcal{A}$ and $\mathcal{B}$, $\mathcal{A}$ and $\mathcal{B}$ will get 0.511 and 0.489 units of rewards on average when both participants use normal inputs. In contrast, when $\mathcal{A}$ uses ADIs, $\mathcal{A}$ will hog all the rewards.

Appendix F: Explore Feature Partition Ratios

Recall in a typical VFL setting where each user ID i has a number of features X, each participant possesses a subset of features. This section studies how the success rate of ADI generation is affected by the feature partition ratio using MNIST and CIFAR-10. We re-run experiments in Table III to compare the dominating rates of standard datasets under various feature partition ratios ("feature" is the number of vertical dimensions of an image). Table XII reports the findings: a feature partition ratio x denotes that $\mathcal{A}$ possesses $x/(1+x)$ percent of the features in each data sample while $\mathcal{B}$ has the rest. To be fair, we initialize all hyperparameters to the same value as Table III. The model accuracy on the test dataset is sufficiently high, indicating that models are well-trained.

Higher ratios imply that $\mathcal{A}$ holds more features. Table XII reports that when more features are allocated to a participant, more ADIs are likely found on its side and dominate others. For instance, for MNIST dataset, when the ratio reaches 2.11 (i.e., $\mathcal{A}$ holds 19 columns while $\mathcal{B}$ holds 9 columns of the image), the dominating rate is 72.40%, indicating that even without perturbation, 72.40% of $\mathcal{A}$'s normal inputs can control the inference. When the ratio falls below 0.65 ($\mathcal{A}$ holds less than 8 columns), none of the original data samples in $\mathcal{A}$ can control the inference, whereas data samples in $\mathcal{B}$ dominate $\mathcal{A}$. When data samples are partitioned evenly (each participant gets 14 columns), the dominating rates on both sides are lower than 1%. For CIFAR-10, we observe similar results that when more features are allocated to a participant, more ADIs are likely found on its side and dominate others. In sum, we view this evaluation reveals a critical observation:



(a) Gradient-based synthesis. (b) Fuzz testing.

Fig. 13: Performance under different feature ratios.

> In VFL, numbers of features allocated on each participant should not largely deviate from each other; by contributing a comparable amount of "knowledge" to the joint inference, the model is seen to be more robust to ADIs.

In contrast, unbalanced feature partitioning causes concerns of dominating inputs and attack opportunities. Fig. 13a reports the success rate of ADI synthesis using different feature partitions. Consistent with Table XII, $\mathcal{A}$ with more features can achieve greater success rates. The success rates are near 100% when the feature partition ratios surpasse 1.8 for MNIST and 1.0 for CIFAR-10. Fig. 13b explores how feature partitioning influences fuzzing. The fuzz testing, consistent with Sec. VII-B, starts with a corpus of 1,000 seeds. We run a 12-hour fuzzing campaign for each feature partition ratio. We find that when assigning $\mathcal{A}$ with more features, fuzzing can uncover more ADIs. For CIFAR-10, we also observe that when the feature partition ratio is greater than 1.33, the number of found ADIs increases much slower. We deem that this is because we use a fixed amount of initial seeds, i.e., $1,000$. Therefore, the number of found ADIs is likely to converge around $1,000$.

VFL faces serious ADI issues when feature partitioning is largely unbalanced. To understand the root cause, assuming $\mathcal{A}$ and $\mathcal{B}$ hold feature partition dimensions d_1 and d_2 as their inputs where d_1 is notably larger than d_2. The mutation V_{d_1} and V_{d_2} are performed on inputs of $\mathcal{A}$ and $\mathcal{B}$, respectively. The parameters of $\mathcal{A}$ and $\mathcal{B}$ are $\theta_{\mathcal{A}_{d_1}}$ and $\theta_{\mathcal{B}_{d_2}}$. According to our observation, for $\mathcal{A}$ holding d_1 and $\mathcal{B}$ holding d_2 dimension of features, their parameters are roughly the same order of magnitude, meaning that $\frac{||\theta_{\mathcal{A}_{d_1}}||_2}{d_1} \approx \frac{||\theta_{\mathcal{B}_{d_2}}||_2}{d_2}$. Thus, the upper bound of $||\theta^T_{\mathcal{A}_{d_1}} V_{d_1}||_1$ is: $||\theta^T_{\mathcal{A}_{d_1}} V_{d_1}||_1 \leq ||V_{d_1}||_2 \times ||\theta_{\mathcal{A}_{d_1}}||_2$. Similarly, $||\theta^T_{\mathcal{B}_{d_2}} V_{d_2}||_1 \leq ||V_{d_2}||_2 \times ||\theta_{\mathcal{B}_{d_2}}||_2$. With $||V_{d_1}||_2 = ||V_{d_2}||_2$, and given d_1 is notably larger than d_2, we have $||\theta_{\mathcal{A}_{d_1}}||_2 > ||\theta_{\mathcal{B}_{d_2}}||_2$. Thus, the upper bound of $||\theta^T_{\mathcal{A}_{d_1}} V_{d_1}||_1$ becomes greater than $||\theta^T_{\mathcal{B}_{d_2}} V_{d_2}||_1$, meaning that the same

TABLE XIII: Dominating rate of the original datasets under different numbers of participants.

Dataset	#Participants	Dominating Rate	Model Accuracy
MNIST	**2**	0.87%	97.78%
	3	0.00%	95.97%
	5	0.00%	97.84%
CIFAR-10	**2**	2.63%	86.55%
	3	0.00%	85.61%
	5	0.00%	85.55%

TABLE XIV: Performance of gradient- and fuzz testing-based algorithms w.r.t. different numbers of participants.

Dataset	#Participants	Gradient Random	Gradient Bounded	Fuzz Testing
MNIST	**2**	92.9%	34.5%	113
	3	56.0%	9.40%	44
	5	48.0%	3.20%	9
CIFAR-10	**2**	99.6%	98.9%	773
	3	83.7%	51.2%	169
	5	64.4%	49.3%	38

mutation ($||V_{d_1}||_2 = ||V_{d_2}||_2$) may have a more significant effect on the output when it is performed on inputs of $\mathcal{A}$ whose dimension d_1 is larger.

Appendix G: Exploring Number of Participants

As introduced in Sec. II, the number of participants in most VFL system designs is two. We now benchmark the attack effectiveness regarding different number of participants. At this step, we use the MNIST and CIFAR-10 datasets and extend the SplitNN protocol for multiple participants (i.e., 3 and 5).

MNIST images are sparse: pixels close to the image corner/border are usually "dark," conveying trivial information. To ensure that image features are partitioned evenly among participants, we divide an image into columns based on the average numbers of pixels greater than zero in each column. This way, to partition images for three participants, $\mathcal{A}$ receives the leftmost 11 columns, participant $\mathcal{B}_1$ gets the middle six, while participant $\mathcal{B}_2$ gets the rightmost 11. For five participants, $\mathcal{A}$ gets the leftmost eight, $\mathcal{B}_{1-3}$ equally split the next 12 columns, and $\mathcal{B}_4$ gets the rightmost eight. For CIFAR-10, we evenly distribute the embeddings of the VGG16 outputs to 3 and 5 participants.

We take 95% as the threshold for this study. We report model accuracy and dominating rates of $\mathcal{A}$'s normal inputs in Table XIII. We interpret $\mathcal{A}$'s normal inputs have a trivial dominating rate, which is consistent with our findings in Table III. We further report the performance of ADI synthesis and fuzzing in Table XIV. Because data features are evenly partitioned among participants, the dimension of data features held by $\mathcal{A}$ shrinks as #participants grows. Thus, the second and third columns of Table XIV show substantially lower success rates. Similarly, fuzz testing finds fewer ADIs in 12 hours. Having more participants means having fewer features allocated to each (malicious) participant. That is, the findings in Table XIV are consistent with those in Table XII and Appx. F. Theoretically, the unbounded mutation can always generate an ADI as long as the malicious participant can make non-trivial contributions to the VFL prediction. However, under the bounded mutation strategy, the proportion of features held by the malicious participant will affect the attack success rate. We deem this as less concerned, since VFL's participant number is typically smaller than five (as noted in Sec. II). Thus, we deem that the bounded mutation will be generally applicable for VFL under different settings.

Appendix H: Multiple Malicious Participants

As stated in Sec. II, unlike HFL, most VFL research designs a VFL system with two participants (maximum four). Hence, we regard only one participant as malicious; this is a practical and stealthy setting. Considering the case where multiple participants are malicious and use ADIs simultaneously (they are not collaborative), it is likely that one of them will dominate the inference results. Here, the same setting as in Sec. VII-A are used to synthesize ADIs on MNIST for $\mathcal{B}$. Then, we let $\mathcal{A}$ and $\mathcal{B}$ both use ADIs, and observe that all the outputs are dominated by either $\mathcal{A}$ or $\mathcal{B}$ (about 70% outputs dominated by $\mathcal{B}$ and the remaining dominated by $\mathcal{A}$).

We also run experiments when there are normal participants and multiple attackers on MNIST and CIFAR-10. Specifically, we first consider three participants, where two participants ($\mathcal{A}$ and $\mathcal{B}$) input ADIs and the other participant inputs normal data during inference. We found that on MNIST, 98.67% of the output results are dominated by either $\mathcal{A}$ or $\mathcal{B}$. Particularly, 45.87% of the results are dominated by $\mathcal{A}$, while the remaining are dominated by $\mathcal{B}$. On CIFAR-10, 96.45% of the output results are dominated by either $\mathcal{A}$ or $\mathcal{B}$, with 65.61% of the results dominated by $\mathcal{A}$ and the rest by $\mathcal{B}$.

Furthermore, we then consider five participants, where two ($\mathcal{A}$ and $\mathcal{B}$) input ADIs, and the other three participants input normal data during inference. We found that on MNIST, 93.48% of the output results are dominated by either $\mathcal{A}$ or $\mathcal{B}$. Particularly, 43.24% of the results are dominated by $\mathcal{A}$, and the rest are dominated by $\mathcal{B}$. On CIFAR-10, 90.38% of the results are dominated by either $\mathcal{A}$ or $\mathcal{B}$, with 43.22% of the results dominated by $\mathcal{A}$ and the rest by $\mathcal{B}$.

We observed that the ratio of the dominated outputs is lower compared with the 3-participant setting (93.48% vs. 98.67% and 90.38% vs. 96.45%). The reason is that in the 5-participant setting, the attackers control fewer features compared to the 3-participant setting. Also, synthesizing ADIs assumes that the other participants will input normal data during inference. When multiple attackers simultaneously input ADIs, such assumptions do not hold anymore. Thus, it is possible that the results are not dominated by any of the attackers' ADIs. And we observe that when the attackers hold more features, their ADIs are more likely to dominate the inference. This observation is consistent with our results in Appx. F and Appx. G.

Overall, the dominating observation could be influenced by the local model, the feature importance, and factors that can affect the ADI generation process, such as $|\mathcal{S}|$. See our study on feature partition ratios and $|\mathcal{S}|$ in Appx. F and Appx. D.

APPENDIX I: TRAINING AND IMPLEMENTATION DETAILS OF LEARNING PROTOCOLS

HeteroLR. Given n training samples X_i whose label is $y_i \in \{0, 1\}$ and coefficient vector θ, logistic regression can be described in a basic form as follows:

$$\mathbb{P}(y_i = 1|X_i, \theta) = h_\theta(X_i) = \frac{1}{1 + e^{-\theta^T X_i}} \tag{12}$$

In typical VFL settings, X_i is partitioned as $[X^i_{\mathcal{A}}||X^i_{\mathcal{B}}]$, while θ is partitioned as $[\theta_{\mathcal{A}}||\theta_{\mathcal{B}}]$. Therefore, HeteroLR in VFL can be formulated as follows:

$$\begin{aligned}\mathbb{P}(y_i = 1|X^i_{\mathcal{A}}, X^i_{\mathcal{B}}, \theta_{\mathcal{A}}, \theta_{\mathcal{B}}) &= h_{\theta_{\mathcal{A}},\theta_{\mathcal{B}}}(X^i_{\mathcal{A}}, X^i_{\mathcal{B}}) \\ &= \frac{1}{1 + e^{-\theta^T_{\mathcal{A}} X^i_{\mathcal{A}} - \theta^T_{\mathcal{B}} X^i_{\mathcal{B}}}}\end{aligned} \tag{13}$$

whose training objective is to minimize the loss function:

$$\begin{aligned}\mathbb{L}_\theta = -\frac{1}{n}\sum_{i=1}^{n} & y_i \, log(h_{\theta_{\mathcal{A}},\theta_{\mathcal{B}}}(X^i_{\mathcal{A}}, X^i_{\mathcal{B}})) \\ & + (1 - y_i) \, log(1 - h_{\theta_{\mathcal{A}},\theta_{\mathcal{B}}}(X^i_{\mathcal{A}}, X^i_{\mathcal{B}}))\end{aligned} \tag{14}$$

We have introduced the general procedure of HeteroLR in background section. At the training stage, when computing gradients, Taylor approximation and homomorphic encryption scheme can be utilized to make training more efficient. To make a joint inference for user ID i, $\mathcal{C}$ collects local prediction results $\theta^T_{\mathcal{A}} X^i_{\mathcal{A}}$ and $\theta^T_{\mathcal{B}} X^i_{\mathcal{B}}$. It then computes and sends the probability $\frac{1}{1+e^{-\theta^T_{\mathcal{A}} X^i_{\mathcal{A}} - \theta^T_{\mathcal{B}} X^i_{\mathcal{B}}}}$ back to $\mathcal{A}$ and $\mathcal{B}$. Note that all the intermediate data is encrypted.

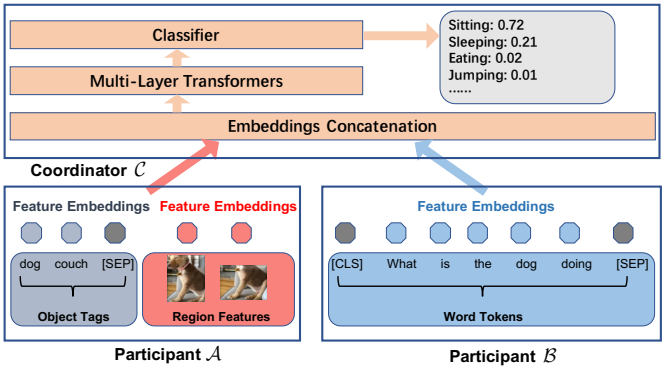


Fig. 14: Architecture of VFVQA.

VFVQA. Visual Question Answering [10], a popular multimodal learning task, answers open-ended natural-language questions about images. VQA models develop a joint understanding of questions and images and have been employed in privacy-sensitive scenarios like medical image diagnosis [7, 61]. VFL provides a practical and effective solution to facilitate privacy-preserving VQA [58]. In our evaluation, we modify the state-of-the-art VQA model Oscar [56] and construct VFVQA as illustrated in Fig. 14.

As introduced in background section, VFVQA concretizes and extends the SplitNN protocol, which involves considerable engineering efforts to link with several modern computer vision and natural language processing models. $\mathcal{A}$ holds the image data and their associated object tags. It computes the feature representation of data using FasterRCNN [79] and BERT [56], where $X_{\mathcal{A}_1}$ and $X_{\mathcal{A}_2}$ represent the image data and the corresponding tags, respectively. $\mathcal{B}$ holds the textual data (i.e., "questions" in VQA) and computes the embedding results of each question using BERT. In particular, $\mathcal{A}$ holds the image data and their associated object tags. It uses FasterRCNN [79] and BERT [56] to process $X_{\mathcal{A}_1}$ and $X_{\mathcal{A}_2}$, corresponding to images and tags. $\mathcal{B}$ process the textual data (i.e., "questions" in VQA tasks) using BERT:

$$\begin{aligned}L_{\mathcal{A}} &= [FasterRCNN(X_{\mathcal{A}_1}, w_{\mathcal{A}_1}) \,||\, BERT(X_{\mathcal{A}_2}, w_{\mathcal{A}_2})] \\ L_{\mathcal{B}} &= BERT(X_{\mathcal{B}}, w_{\mathcal{B}})\end{aligned} \tag{15}$$

As specified by the SplitNN protocol, local results on each participant are sent to the coordinator $\mathcal{C}$. Then, $\mathcal{C}$ predicts the answer, another natural language sentence, to the raised question on $\mathcal{B}$ based on the image feature shared by $\mathcal{A}$ using multi-layer transformers:

$$L_{\mathcal{C}} = Transformer([L_{\mathcal{A}} \,||\, L_{\mathcal{B}}], w_{\mathcal{C}}) \tag{16}$$

The backward propagation phase is performed consistently with SplitNN. And all intermediate data in the above phases are encrypted.

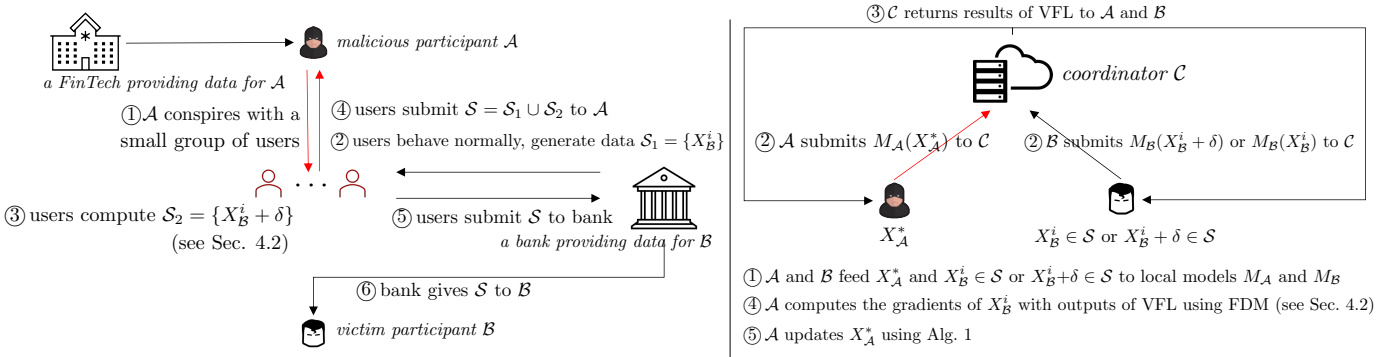
APPENDIX J: PIPELINE OF BLACKBOX ADI SYNTHESIS

In this section, we present an end-to-end illustration of ADI synthesis in the blackbox setting. We consider the VFL example given in Sec. I, where a FinTech and a bank jointly predict a user's credit score. Before launching the attack and synthesizing ADIs, we assume that a VFL system has been well trained, where $\mathcal{A}$ takes training data from the FinTech and $\mathcal{B}$ takes the training data from the bank.

Fig. 15a depicts the procedure of collecting $\mathcal{S}$, whose high-level procedure has been mentioned in Sec. III-B. In particular, the malicious participant $\mathcal{A}$ conspires with a small group of users: these users behave normally, but are willing to share their records in the bank with $\mathcal{A}$ (①). These users behave *normally* and register their information in the bank. Their provided bank records will form our target sample dataset $\mathcal{S}_1$ (②). Then, as discussed in Sec. IV-B, these users further compute another collection of bank records, by adding permutation δ to each bank record $X^i_{\mathcal{B}} \in \mathcal{S}_1$. These $X^i_{\mathcal{B}} + \delta$ form another sample dataset $\mathcal{S}_2$ (③). Given that users are conspiring with $\mathcal{A}$, both $\mathcal{S}_1$ and $\mathcal{S}_2$ are shared with $\mathcal{A}$ (④). Similarly, $\mathcal{S}_2$ will need to be provided to the bank, and therefore, both $\mathcal{S}_1$ and $\mathcal{S}_2$ are accessible to $\mathcal{B}$ (⑤, ⑥).The tiny collection of data samples $\mathcal{S}$ is formed by $\mathcal{S}_1$ and $\mathcal{S}_2$: $\mathcal{S} = \mathcal{S}_1 \cup \mathcal{S}_2$.

With $\mathcal{S}$ becomes accessible to both $\mathcal{A}$ and $\mathcal{B}$, $\mathcal{A}$ can start to synthesize ADIs via estimated gradients (see Sec. IV-B). Fig. 15b shows the pipeline of our blackbox ADI synthesis.

Typically, before launching a joint inference, $\mathcal{C}$ will coordinate and inform $\mathcal{A}$ and $\mathcal{B}$ about the user ID. Thus, $\mathcal{A}$ can easily decide whether the current input of $\mathcal{B}$ is from the sample set $\mathcal{S}$ according to the current user ID. If so, $\mathcal{A}$ can start to update its ADI input $X^*_{\mathcal{A}}$. To do so, $\mathcal{A}$ feeds ADI $X^*_{\mathcal{A}}$ to local model $M_{\mathcal{A}}$ and $\mathcal{B}$ feeds $X^i_{\mathcal{B}} \in \mathcal{S}$ or $X^i_{\mathcal{B}} + \delta \in \mathcal{S}$ to local model $M_{\mathcal{B}}$



(a) Procedure of collecting $\mathcal{S}$.

(b) Pipeline of blackbox ADI synthesis.

Fig. 15: Pipeline of Blackbox ADI Synthesis.

and get the corresponding outputs (①). Then, $\mathcal{A}$ and $\mathcal{B}$ submit their local outputs to $\mathcal{C}$ and receive the joint inference output of the VFL model from $\mathcal{C}$ (② and ③). Then, as we discuss in Sec. IV-B, $\mathcal{A}$ can compute the gradients of $X^i_{\mathcal{B}} \in \mathcal{S}$ by FDM (④). Finally, $\mathcal{A}$ updates ADI $X^*_{\mathcal{A}}$ by Alg. 1 without accessing the local model of $\mathcal{B}$ (⑤).

Appendix K: Cooperating Fuzz Testing with VFL Protocols

As reported in evaluation section, we launch fuzz testing toward two widely-used VFL protocols (i.e. HeteroLR and SplitNN) on the basis of real-world VFL platforms FATE and FedML. We also launch fuzz testing toward VFVQA, whose protocol is consistent with SplitNN. A detailed procedure to cope with fuzz testing with learning protocols is given in Table XV. In all, greybox fuzzing can be accordingly performed on the distributed versions of learning protocols without sharing much information about the original data.

Appendix L: Datasets Information

We use six popular datasets in our evaluation Sec. VII: NUS-WIDE [25], Credit [1], Vehicle [6], MNIST [52], VQA v2.0 [57], and CIFAR-10 [51]. NUS-WIDE dataset contains 269,648 images and the associated tags. Each sample has 634 low-level image features and 1,000 text features. Thus, it is suitable for a feature-partition setting and is therefore commonly used to benchmark VFL. We set up a joint classification task of ten labels via two participants $\mathcal{A}$ and $\mathcal{B}$. We use the top ten labels in NUS-WIDE having the maximum number of data samples. $\mathcal{A}$ holds the image features whereas $\mathcal{B}$ holds the text features.

Credit dataset is a popular benchmark dataset for VFL that comprises the payment records of 30,000 customers of a bank, where 5,000 customers are malicious while the rest are benign. Each data sample has 23 integer or floating-point number features. We set up a VFL logistic regression task over participants $\mathcal{A}$ and $\mathcal{B}$ to predict whether a payment is from a malicious customer or not. Participant $\mathcal{A}$ holds 13 features and participant $\mathcal{B}$ holds 10.

Vehicle dataset is a multi-classification dataset containing 946 samples of four vehicle categories. Each sample has 18 features. We set up a VFL logistic regression task over two participants $\mathcal{A}$ and $\mathcal{B}$ to classify data samples into the vehicle categories. Both $\mathcal{A}$ and $\mathcal{B}$ get nine features each.

MNIST is a handwritten digital image dataset with 60,000 training samples and 10,000 testing samples, each with dimensions of 28×28 pixels. We set up a VFL classification task with ten labels over participants $\mathcal{A}$ and $\mathcal{B}$. Each image is vertically partitioned into two such that $\mathcal{A}$ gets the left piece (with 28×14 pixels) while $\mathcal{B}$ gets the right piece.

VQA v2.0 is a large-scale dataset widely used to train VQA models. We set up VFVQA over participants $\mathcal{A}$ and $\mathcal{B}$ to facilitate VQA, where $\mathcal{A}$ holds images and $\mathcal{B}$ raises natural-language questions. There are 82,783 images and 443,757 questions in the training set, and 40,504 images and 214,354 questions in the validation set. The images are embedded as a feature vector of size 2,054 while the questions are embedded as a word embedding matrix with shape 128×512.

CIFAR-10 is a relatively complex colour image dataset with 50,000 training samples and 10,000 testing samples, each with dimensions of $32 \times 32 \times 3$ pixels. There are 10 labels for this dataset. Similar to MNIST, we set up a VFL classification task with 10 labels iver participants $\mathcal{A}$ and $\mathcal{B}$. Each image is vertically partitioned into two, such that $\mathcal{A}$ gets the left piece and $\mathcal{B}$ gets the right piece. $\mathcal{A}$ and $\mathcal{B}$ use VGG16 to get a feature embedding with 10,752 dimensions and use the embeddings as the inputs for the VFL model.

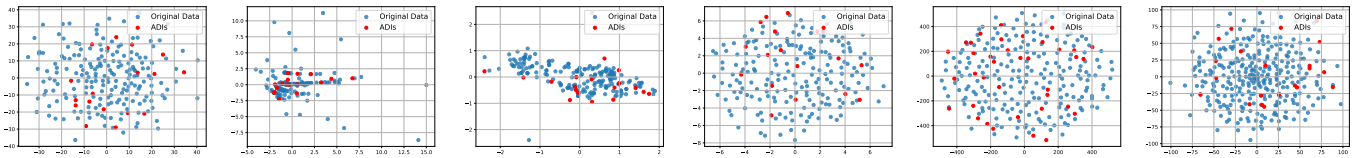
Appendix M: Fuzz Testing Results Visualization

The ADIs generated by fuzz testing and original inputs of participant $\mathcal{A}$ are projected to 2D figures by multidimensional scaling. As shown in Fig. 16, the ADIs are distributed close to the original data. We interpret that the generated ADIs (marked in red) are *stealthy*: they can be hardly distinguished by the data distribution nor by the distances between the data points.

We also present several MNIST cases generated by fuzz testing in Fig. 17. Similar to Fig. 8, we report the ADIs used by $\mathcal{A}$, the normal inputs used by $\mathcal{B}$, and also the corresponding saliency maps. It is easy to see that ADIs on $\mathcal{A}$ dominate the joint inference, and make the contribution of $\mathcal{B}$ negligible.

TABLE XV: Detail steps to cooperate fuzz testing with the VFL protocols.

	Participant $\mathcal{A}$	**Participant $\mathcal{B}$**	**Coordinator $\mathcal{C}$**
1.	Generate index Seeds **S**, maintain a list **Q** storing the corresponding data.	Compute all local results of data in participant $\mathcal{B}$, send to $\mathcal{C}$	
2.	a) Choose next from **S** as $index_a$. b) Add noise to **Q**[$index_a$] for β times. c) Compute local results of the noised data, send to $\mathcal{C}$.		
3.			a) Randomly choose a local result of participant $\mathcal{B}$ and the corresponding index is $index_b$. b) Compute the outputs of all noised data and gradients, send to $\mathcal{A}$ and $\mathcal{B}$.
4.	Compute the saliency score of all noised data, send the highest $saliency_score_a$ and corresponding $index_noise_a$ to $\mathcal{C}$.	Compute the $saliency_score_orig_b$, send to $\mathcal{C}$.	
5.			Compute Attack Success Rate, send to $\mathcal{A}$.
6.	a) Maintain the $orig_acc$. b) Compute the Saliency Mask based on the gradients received. c) Compute $data_noise_mask_a$ based on the Mask. d) Compute the local result of $data_noise_mask_a$, send to $\mathcal{C}$.		
7.			Compute output, gradients and Attack Success Rate ($masked_acc$), send to $\mathcal{A}$ and $\mathcal{B}$.
8.	Compute $saliency_score_masked_a$, send to $\mathcal{C}$.	Compute $saliency_score_masked_b$, send to $\mathcal{C}$.	
9.			Compute $ratio_a$ = $saliency_score_masked_a$ / $saliency_score_orig_a$ and $ratio_b$ = $saliency_score_masked_b$ / $saliency_score_orig_b$, send to $\mathcal{A}$.
10.	If $masked_acc > orig_acc$ and $ratio_a > ratio_b$, update **Q**[$index_a$] = $data_noise_mask_a$. If $masked_acc >$ threshold, add **Q**[$index_a$] to $\mathcal{A}$, delete $index_a$ from **S** and return to Step 2.		
11.	Return to step 3 for γ times.		
12.	Return to step 2 for Γ times.		



(a) NUS-WIDE. (b) Credit. (c) Vehicle. (d) MNIST. (e) VQA v2.0. (f) CIFAR-10.

Fig. 16: Normal inputs and ADIs generated by fuzz testing projected to 2D figures.

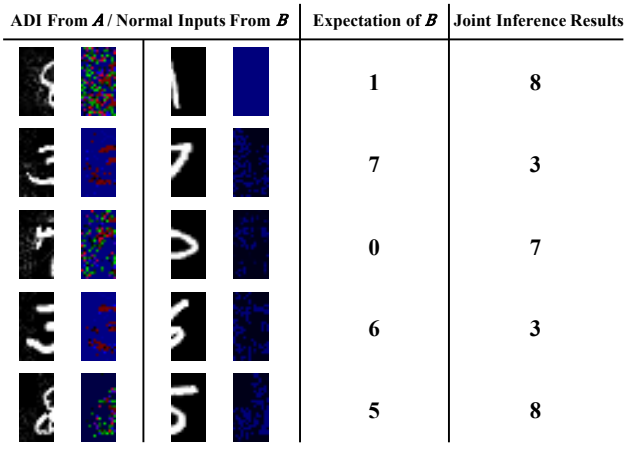


Fig. 17: ADIs found in MNIST using fuzz testing.